

Author Response

The replies are as published on the discussion page, but are repeated here:

We thank the reviewers for their comments and suggestions.

We repeat the comments below in italic and then add our replies to this.

Reviewer 1

General comments: This paper is an important contribution, presenting quantitative estimates of dehydration effects of contrails at flight levels and release of water after ice particle advection and sedimentation. Individual contrails are simulated by coupling a plume-scale contrail model with a global aerosol–climate model. Statistical contrail ensemble properties are as expected from present understanding and consistent with available observations. The radiative forcing from contrails and dehydration is estimated. Many results are new and important for understanding total effect on climate by aircraft. The manuscript is well written and the results are clearly presented. I recommend that this paper is published with minor revisions. There are only a few suggestions for revisions as described below.

Thank you for this positive general comment.

Minor points: Figs. 3 and 4: According to the manuscript, these figures are wrongly interchanged.

Thank you. Now corrected.

Page 19573, line 14: Definition of “cirrus” cloud is ambiguous because many definitions are present in the literature. Particularly, it is not clear whether it includes sub-visual cirrus, thin and opaque cirrus clouds. Optical thickness range should be explained for clarity.

We agree, the definition of cirrus cover is critical. CAM computes the cover of cirrus as a function of ice supersaturation as described in Wang and Penner (2010), without reference to optical depth. Hence, we cannot specify a threshold value of optical depth for the CAM result. The observations, as summarized in Stubenrauch et al. (2013), depend strongly on the method used (passive nadir sensors give smaller coverage than limb sounders and lidar). These are important aspects, but go beyond the scope of this paper concentrating on contrails. Hence, we rewrite the first sentence of our subsection 3.1.1.f as follows:

Figure 11 shows the annual mean global cirrus and contrail cover. The mean cirrus cover computed in these simulations by CAM is 40%. The value of cloud cover depends critically on the method used, and is specified here as a function of assumed probability density function of supersaturation within each grid (Wang and Penner, 2010). The result is roughly consistent with a range of satellite observations of thin and opaque high-level clouds (Stubenrauch et al., 2013).

Page 19573, line 22: Authors describe differences of estimated contrail cover from previous estimates in detail and suggest possible reasons, but it is not clear whether the 5-times larger contrail cover a better estimate than previous ones.

The text says: The computed contrail cover is about 5 times larger than derived from linear contrails in satellite data (Palikonda et al., 2005; Meyer et al., 2007).
The total contrail cover is larger than the one observed for linear contrails. That should be self-explaining. No change.

Page 19578, Line 5: A typo, “variably”, should be “variability”

Thank you. Now corrected.

Reviewer 2

This study addresses an important question concerning the redistribution of humidity in the atmosphere by contrails at global scale. By coupling a climate model with a contrail model, it quantifies the effect of dehydration on the radiative effect of contrails and of the redistribution of humidity in the atmosphere. The authors report a small negative net radiative forcing from dehydration related to a reduction of the liquid and ice water paths and cloud cover of low and high-level clouds. The manuscript is clearly structured and presented, and I recommend its publication in its present version, with very minor suggestions.

Thank you for this positive general comment.

Figures 3 and 4 seem to have been swapped.

Thank you. Now corrected.

Page 19575, line 6: The authors mention some factors that affect contrail RF, to which contrail lifetime and diurnal variation should be added, as these factors play a crucial role in the balance between the SW and LW contrail forcing contributions.

We wrote: „Moreover, the RF values depend on the radiances without contrails, cloud temperatures, optical ice particle properties, cloud overlap, and 3-D effects (Meerkötter et al., 1999; Markowicz and Witek, 2011; Forster et al., 2012; Yi et al., 2012).“

We change this as follows:

„Besides on contrail life times and diurnal variations, the RF values depend on the radiances without contrails, cloud temperatures, optical ice particle properties, cloud overlap, ice water path, and 3-D effects (Meerkötter et al., 1999; Markowicz and Witek, 2011; Forster et al., 2012; Yi et al., 2012; De Leon et al., 2012).“

Further reference:

De Leon, R. R., Krämer, M., Lee, D. S., and Thelen, J. C.: Sensitivity of radiative properties of persistent contrails to the ice water path, Atmos. Chem. Phys., 12 7893-7901, 2012.

Page 19582, paragraph 3: The authors correctly highlight the dependence of their results on the representation of sedimentation and the contrail’s particle size spectrum. It would be interesting if they could also comment on the dependence of the radiative properties on these factors.

When saying that the results depend on sedimentation, then we refer to the results in total, including radiative properties. We have no specific information to add on this point at this place.

However, we now mention the sensitivity to ice water path by a further reference to De Leon et al. (2012) in the changes of the sentence on Page 19575, line 6, as given above.

We also change two minor spelling errors (plural instead of singular) and edited two figures (two numbers with decimal point instead of comma, in the legend of Fig 4, formerly fig. 3; and a color change in Fig. 9 for clarity.)

We have prepared a changed Latex text file which contains these changes based on the last available tex file of the acpd text. We plan to email this to Copernicus when the paper got accepted.

Besides the manuscript we submit two new eps-file figures.

2
3 **Dehydration effects from contrails in a coupled contrail-climate model**

4
5 **U. Schumann¹, J. E. Penner², Y. Chen², C. Zhou², and K. Graf¹**

6 ¹Deutsches Zentrum für Luft- und Raumfahrt, Institut für Physik der Atmosphäre,
7 Oberpfaffenhofen, Germany

8 ²University of Michigan, Department of Atmospheric, Oceanic, and Space Sciences, Ann
9 Arbor, Michigan, USA

10 Correspondence to: U. Schumann (ulrich.schumann@dlr.de)

11
12 **Abstract**

13 Uptake of water by contrails in ice-supersaturated air and release of water after ice particle
14 advection and sedimentation dehydrates the atmosphere at flight levels and redistributes
15 humidity mainly to lower levels. The dehydration is investigated by coupling a plume-scale
16 contrail model with a global aerosol-climate model. The contrail model simulates all the
17 individual contrails forming from global air traffic for meteorological conditions as defined
18 by the climate model. The computed contrail-cirrus properties compare reasonably with
19 theoretical concepts and observations. The mass of water in aged contrails may exceed 10^6
20 times the mass of water emitted from aircraft. Many of the ice particles sediment and release
21 water in the troposphere, on average 700 m below the mean flight levels. Simulations with
22 and without coupling are compared. The drying at contrail levels causes thinner and longer
23 lived contrails with about 15 % reduced contrail radiative forcing (RF). The reduced RF from
24 contrails is of the order 0.06 W m^{-2} , slightly larger than estimated earlier because of higher
25 soot emissions. For normal traffic, the RF from dehydration is small compared to interannual
26 variability. A case with 100 times increased emissions is used to overcome statistical
27 uncertainty. The contrails impact the entire hydrological cycle in the atmosphere by reducing
28 the total water column and the cover of high and low-level clouds. For normal traffic, the
29 dehydration changes contrail RF by positive shortwave and negative longwave contributions

30 of order 0.04 W m^{-2} , with a small negative net RF. The total net RF from contrails and
31 dehydration remains within the range of previous estimates.

32

33

34 **1 Introduction**

35 Contrail ice particles grow by uptake of humidity from ambient ice-supersaturated air masses
36 and release their water content after sedimentation or advection with the wind into regions
37 with lower relative humidity. *Knollenberg* [1972] derived the ice mass inventory in a contrail
38 for a single aircraft from measurements and found that there are at least four orders of
39 magnitude more water present as ice in the contrail than in the original aircraft exhaust.

40 Hence, contrails dry or dehydrate the atmosphere at places where they form, and redistribute
41 humidity to places in the atmosphere where they sublimate [*Fahey and Schumann, 1999*].

42 Small relative changes of humidity in the troposphere and small absolute changes in the
43 tropopause region have large effects on radiative forcing [*Riese et al., 2012*]. Ice is far more
44 efficient in radiative forcing than water vapor [*Meerkötter et al., 1999; Chen et al., 2000;*
45 *Fusina et al., 2007; Wilcox et al., 2012*]. The redistribution of humidity may make contrails
46 thinner. In regions with heavy air traffic, contrail-cirrus persistence can modify or even
47 suppress natural cirrus formation [*Unterstrasser, 2014*], with consequences for radiative
48 forcing [*Burkhardt and Kärcher, 2011*]. Falling ice particles may enhance precipitation from
49 mixed-phase or warm clouds at lower altitudes, by increasing humidity and thus the liquid
50 water content or by the Wegener-Findeisen-Bergeron process, both of which are thought to
51 increase the likelihood of precipitation [*Murcray, 1970; Korolev and Mazin, 2003; Yun and*
52 *Penner, 2012*]. Dehydration from contrails may follow similar processes as dehydration by
53 thin cirrus at the tropical tropopause [*Jensen et al., 1996; Fueglistaler et al., 2009*].

54 Contrails have been investigated in many observational and numerical studies [*Schumann,*
55 *2002; Mannstein and Schumann, 2005; Burkhardt et al., 2010; Heymsfield et al., 2010; Yang*
56 *et al., 2010; Unterstrasser and Gierens, 2010b; Minnis et al., 2013; Lewellen, 2014; Voigt et*
57 *al., 2015*]. Nevertheless, the dehydration effects from contrails are not well known. Previous
58 assessments of the climate impact of aviation [*Schumann, 1994; Brasseur et al., 1998; Penner*
59 *et al., 1999; Sausen et al., 2005; Lee et al., 2009; Lee et al., 2010; Boucher et al., 2013;*
60 *Brasseur et al., 2015*] discussed the dehydration effects from contrails qualitatively.

61 *Burkhardt and Kärcher* [2011] were the first to quantify the dehydration effects within a
62 global climate model. Contrail formation was treated as a subgrid-scale (SGS) process which

63 included a separate cloud class for young contrails. They found that contrail cirrus causes a
64 significant decrease in natural cloudiness, which partly offsets their warming effect. They
65 estimated the cooling from reduced cirrus at about 7 mW m^{-2} and called for further work to
66 more reliably quantify this effect.

67 Observations show ice particles precipitating from contrails in ice supersaturated air
68 [Heymsfield *et al.*, 1998] and ~ 2 km deep fall streaks of quickly falling large ice particles
69 below individual contrails at horizontal scales of ~ 5 km, far smaller than global model grid-
70 scales [Schumann, 1994; Atlas *et al.*, 2006]. Details of fall streaks below individual contrails
71 were simulated in large-eddy simulations (LES) [Jensen *et al.*, 1998; Unterstrasser *et al.*,
72 2012]. Such fall streaks could not appear if the cirrus clouds are represented by mean values
73 in the large grid cells of a global model. Obviously, the large scale separation between
74 individual contrails and global scales makes it difficult to assess the global impact of
75 dehydration from contrails.

76 A contrail prediction model CoCiP has been developed to simulate the formation and decay of
77 all individual contrail segments for given air traffic and ambient meteorology [Schumann,
78 2012] including contrail induced radiative forcing [Schumann *et al.*, 2012b]. CoCiP uses a
79 simplified model designed to approximate the essential contrail physics for efficient
80 simulation of contrails from global traffic over long periods. The contrail model bridges the
81 scales from the aircraft wake to the global atmosphere. Various of the model results compare
82 reasonably with observations [Voigt *et al.*, 2010; Schumann, 2012; Jeßberger *et al.*, 2013;
83 Schumann and Graf, 2013; Schumann *et al.*, 2013a]. In the past, the model has been run in an
84 offline mode for given meteorological fields, without exchange of humidity between contrails
85 and background air.

86 In this study, the contrail model is coupled with the global climate model CAM3+/IMPACT
87 [Wang and Penner, 2010], here also called CAM. The global model includes complex
88 aerosol-cloud interactions, cirrus and ice supersaturation. The coupled CoCiP/CAM model is
89 applied to quantify the impact of water exchange on contrail properties, large scale humidity
90 distribution, and background climate. In order to isolate the effects of water uptake by ice
91 particles without complicating effects from soot and other aerosols [Penner *et al.*, 2009;
92 Hendricks *et al.*, 2011; Gettelman and Chen, 2013; Righi *et al.*, 2013], this study is purposely
93 restricted to the effects from exchanges of water. The ice nucleation properties of soot from
94 aviation emissions might get changed when entering contrail ice [Zhou and Penner, 2014].
95 This is a possibly important effect which should be included in a future model application.

96 For small climate disturbances, to which aviation effects belong, the analysis of climate
97 impact from free running climate simulations is hampered by the noise inherent in such
98 climate models because of the chaotic nature of atmosphere dynamics. For a climate model
99 study with a diagnostic linear contrail model, *Ponater et al.* [2005] used a factor of 20 larger
100 fuel consumption and *Rap et al.* [2010a] used 100 times enhanced contrail optical depth, to
101 obtain statistically significant results from 30- to 50-year climate simulations. This is a valid
102 approach as long as the climate response to the disturbances is about linear. *Gottelman and*
103 *Chen* [2013] and *Chen and Gottelman* [2013] were able to reduce the climate noise using a
104 20-year climate model (CAM5) simulation nudged to the pressure, winds and atmospheric
105 and sea surface temperatures from a previous one-year simulation. In order to quantify the
106 effects from this “nudging”, one would need comparisons with and without nudging. Here, we
107 try to overcome climate noise by using enhanced emissions and estimate the linearity of the
108 responses.

109 **2 Methods**

110 **2.1 CAM3+ /IMPACT model**

111 The method is a new combination of CoCiP with CAM3+/IMPACT, with code changes to
112 allow for coupling with exchange of water between contrails and ambient air.
113 CAM3+/IMPACT is an updated version of the coupled aerosol-general circulation model
114 described in *Wang and Penner* [2010] and *Yun et al.* [2013]. CAM3 is the Community
115 Atmosphere Model version 3, which simulates the atmosphere. Here, it is run using fixed sea
116 surface temperature climatology with an overall time step of 1 h and spatial resolution of 2° in
117 latitude and 2.5° in longitude with 26 vertical model levels up to about 3.5 hPa. IMPACT is
118 the University of Michigan aerosol model, which treats a total of 17 aerosol types [*Zhou and*
119 *Penner*, 2014]. The model used here combines features added to CAM3 (called CAM3+) by
120 *Liu et al.* [2007], *Wang and Penner* [2010], *Yun and Penner* [2012] and *Yun et al.* [2013].
121 CAM3+ uses a two-moment cloud microphysics scheme for cloud ice, in which mass and
122 number concentrations are predicted by prognostic equations. The two-moment scheme treats
123 ice nucleation, evaporation, and melting, and allows for ice supersaturation. The cloud
124 fraction calculation accounts for new cloud cover by ice nucleation, treating homogeneous
125 and heterogeneous nucleation of ice. The surface emissions included are for the year 2000
126 [*Penner et al.*, 2009]. The model has previously been compared with observations [*Yun and*
127 *Penner*, 2012]. E.g., *Wang and Penner* [2010] showed that the model predicts the global

128 distribution of ice supersaturation, cloud cover, ice water content, and ice crystal
129 concentrations in reasonable agreement with observations.

130 **2.2 The contrail simulation model CoCiP**

131 CoCiP is a Lagrangian model which traces individual contrail segments forming along flight
132 routes for many flights. The model is documented and discussed in *Schumann* [2012]. In the
133 following, the major features are explained with a few modifications. CoCiP simulates the
134 lifecycles of contrails from their formation behind individual aircraft until final dissipation.
135 Contrails are assumed to form when the Schmidt-Appleman criterion is satisfied for given
136 ambient temperature and humidity, given fuel (H_2O emission index 1.24, combustion heat
137 43.2 MJ kg^{-1}), and given overall propulsion efficiency [*Schumann*, 1996]. The model assumes
138 that the soot particles emitted into the young exhaust plume act as condensation nuclei for
139 contrail formation when humidity exceeds liquid saturation. The resultant droplets freeze soon
140 thereafter because of ambient temperature below homogeneous freezing limits. In the wake
141 phase, some ice particles get lost by adiabatic warming or by mixing with dry ambient air.
142 The initial contrail properties (depth, width, number of ice particles, initial ice water content)
143 are computed for given aircraft types. (The importance of aircraft size, speed, fuel
144 consumption, and emissions for contrail properties was subject of several recent studies
145 [*Lewellen and Lewellen*, 2001; *Naiman et al.*, 2011; *Voigt et al.*, 2011; *Jeßberger et al.*, 2013;
146 *Schumann et al.*, 2013; *Unterstrasser and Görsch*, 2014]). The contrail advection and the
147 shear and turbulence-driven spreading and mixing of plume air with ambient air are simulated
148 with a Gaussian plume model. Contrails spread vertically mainly by turbulent mixing excited
149 by shear and limited by stable stratification. In the model, particle sedimentation and
150 differential radiative heating contribute to enhanced vertical diffusivity. Shear tends to distort
151 plumes into vertically thin sheets enhancing vertical mixing. Horizontal diffusivities are larger
152 because horizontal motions are not limited by stratification. The contrail bulk ice physics is
153 approximated as a function of ice water content and ice particle number N_{ice} per flight
154 distance assuming saturation inside the contrail, which is justified for dense ice clouds or slow
155 humidity changes [*Korolev and Mazin*, 2003; *Kaufmann et al.*, 2014]. The local ice particle
156 concentration n_{ice} is computed from the number of ice particles per flight distance divided by
157 the plume cross-section. After contrail formation, the contrail ice water content grows by
158 uptake of ambient humidity entering the plume by mixing with ambient ice supersaturated air.
159 When mixing with subsaturated air, the ice water content shrinks accordingly. The number of
160 contrail ice particles is modelled as a function of soot emissions with some parameterized

161 losses during the wake vortex phase of the contrail. The number of ice particles per unit
162 plume length stays constant in the model except for aggregation between contrail particles
163 with cirrus particles, and turbulent mixing losses, which are parameterized. (For a discussion
164 of the aggregation model used, see *Kienast-Sjögren et al.* [2013]). In each contrail segment,
165 the volume mean particle radius r_{vol} is computed from the volume of the ice and the particle
166 number. For local optical depth and RF analysis, an effective radius r_{eff} is computed assuming
167 a fixed value $C=r_{\text{vol}}/r_{\text{eff}}=0.9$ [*Schumann et al.*, 2011b]. The volume-mean ice particle size is
168 used to compute the mean fall speed [*Spichtinger and Gierens*, 2009]. The vertical motion of
169 the contrail follows the sum of ambient vertical velocity and fall speed. Because of crystal
170 size dispersion, sedimentation also contributes to vertical widening of the plume cross-
171 section. The contrails terminate when all ice water content is sublimated (by mixing with dry
172 air, e.g., during subsidence) or by precipitating below the lower boundary of the CoCiP
173 domain. Contrail cover is computed on a fine grid with 5000×3600 longitude \times latitude-grid
174 cells (about 5 km horizontal resolution) based on a threshold of 0.1 for optical depth (at 550
175 nm), accounting for overlapping with other contrails and with ambient cirrus. Hence, a thin
176 contrail overlapping with other thin cirrus may enlarge cover by enhancing the total optical
177 depth beyond the threshold. The radiative forcing (RF) induced by contrails is computed from
178 the sum of the contributions from each contrail; for each contrail, the RF is computed as a
179 function of contrail properties and top of the atmosphere radiances [*Schumann et al.*, 2012b].
180 The model is driven by air traffic waypoint data. Here, we use a global data set for the year
181 2006, including about 80000 flights per day, as provided within the ACCRI project
182 [*Wilkerson et al.*, 2010; *Brasseur et al.*, 2015]. [The data set accounts for the diurnal cycle of](#)
183 [traffic](#). The fuel consumption and the corresponding water emissions from aircraft engines are
184 available with these waypoint data. The overall propulsion efficiency, mostly between 0.2 and
185 0.4, is deduced from the given speed, fuel consumption and thrust. The number of soot
186 particles emitted is set to be proportional to the fuel consumption with fixed emission index
187 ($10 \times 10^{14} \text{ kg}^{-1}$). The emission index used here is larger than in earlier studies ($3.57 \times 10^{14} \text{ kg}^{-1}$)
188 because recent experimental data indicate that modern aircraft emit more (by number) soot
189 particles acting as contrail ice nuclei than estimated earlier [*Schumann et al.*, 2013].

190 CoCiP simulates contrail segments for each flight from departure until arrival for a maximum
191 life time, set to 36 h in this application. (Ages up to about a day have been observed [*Minnis*
192 *et al.*, 1998; *Haywood et al.*, 2009; *Vázquez-Navarro et al.*, 2015]). In the original code
193 version, this required frequent readings of the input files. To reduce computing time, we split
194 the traffic data into hourly data. For each hour of integration over the year, first the contrail

195 segments from the previous flights, if existing, are integrated forward in time over the next
196 hour or until they die out. Thereafter, contrails from the new flight segments occurring during
197 the hour are treated. Contrails remaining active at the end of the time step are saved for the
198 next integration step.

199 The CoCiP model results depend on various critical model parameters; see Table 2 of
200 *Schumann* [2012]. In particular, plume diffusivities are modeled as in *Schumann and Graf*
201 [2013], with vertical plume diffusivities computed for $w'_N = 0.22 \text{ m s}^{-1}$; and the vertical
202 diffusivity is enhanced when radiative heating in the contrails causes convective instability.
203 With respect to particle losses, we found that the second-order Runge-Kutta scheme for
204 integration of the prognostic equations is stable and accurate enough without the need for
205 iterations, reducing computing time. We also found, partially because of a compensating code
206 error in the Runge Kutta scheme, that the loss of particles due to mesoscale fluctuations has a
207 small impact on the results and is no longer required (parameters $E_T=0.1$, $E_{\text{meso}}=0$, see Table 2
208 of *Schumann* [2012]). The humidity seen by CoCiP in the troposphere is assumed to be
209 enhanced by a factor of $1/\text{RH}_c$ ($\text{RH}_c=0.9$) compared to what is provided by the host model to
210 account for SGS variability and possible systematic deviations from observations. In a
211 previous study, we used numerical weather prediction results from the European Center for
212 Medium Range Weather Forecasts (ECMWF) with a SGS factor $\text{RH}_c=0.8$ [*Schumann and*
213 *Graf*, 2013]. From the results of the present study, we learn that $\text{RH}_c=1$ appears to give
214 satisfactory results and should be used in future applications.

215 **2.3 The coupling of CoCiP to CAM**

216 CAM calls CoCiP as a subroutine each time step providing the most recent meteorological
217 fields as input. The fields include three-dimensional (3-D) fields of wind, temperature,
218 humidity, ice water content, and cloud cover as a function of pressure. In addition, two-
219 dimensional fields are provided for surface pressure, outgoing longwave radiation, reflected
220 shortwave radiation, and incoming solar direct radiation. CoCiP interpolates in these fields
221 linearly in space and time to obtain the values at any position.

222 In the offline mode, each contrail segment is simulated for the given ambient meteorological
223 fields without changing background meteorology. This simplification is unavoidable when
224 CoCiP is driven by the output of numerical weather prediction models, as done in the past.
225 The offline mode allows for the efficient simulation of the contrails from millions of flights.
226 For the coupled model, CoCiP is run either offline or online.

227 In the online mode, CoCiP returns effective emissions (besides H₂O, the code can treat also
228 soot emissions) from aircraft after contrail processing. CoCiP accounts for the emissions
229 exchanged between the background atmosphere and the contrails per time step and per CAM
230 grid cell by tracking 3-D-fields EA, EC and CA (the sum of EA and CA is provided as a
231 water source to CAM and treated as given emissions). EA (engine to atmosphere) records the
232 emission amount emitted from aircraft engines directly to the atmosphere, without processing
233 in contrails. EC (engine to contrail) is the amount emitted from aircraft engines into fresh
234 contrails. Positive CA (contrail to atmosphere) values are the amounts released from contrails
235 to the atmosphere, negative CA values are the amounts taken up by contrails from the
236 atmosphere. The emissions are split into EA and EC during contrail formation as a function of
237 the initial ice water content inside the freshly formed contrails relative to the amount of water
238 emitted from the engines. Hence, if no contrail forms, EA from this flight contains all
239 emissions and the contribution to EC is zero. After contrail initiation, in growing contrails, the
240 water contribution to CA becomes negative, because contrail ice grows by uptake of ambient
241 humidity. Later during the contrail life cycle, the contrail provides a positive CA contribution
242 when ice sublimates releasing water to the atmosphere. The local sign of CA depends on the
243 mix of growing and shrinking contrails within the grid cell. For diagnostics, CoCiP records
244 the inventory of the emission amount stored inside contrail particles per CAM grid cell in a
245 further 3-D field as a function of time. The sum of fields EA and CA and this inventory
246 include all aircraft emissions in the CoCiP domain. Hence, the H₂O mass passed between
247 CoCiP and CAM is conserved. To reduce storage requirements, CoCiP operates on a limited
248 altitude domain where contrails form, covering 18 CAM model levels, from 916 to 100 hPa.
249 Aircraft emissions outside this altitude range (e.g., from airports) are included in CAM
250 separately in a consistent manner.

251 To avoid negative vapor concentrations in regions with many contrails forming during a time
252 step, CoCiP accounts for local H₂O exchange between the contrails and background air during
253 the integration time step. For this purpose, CoCiP uses a local copy of the background H₂O
254 concentration field provided by CAM and subtracts from it the amount of water vapor uptake
255 by a contrail (and adds any released contrail water) immediately. The contribution from each
256 contrail segment is distributed over contrail neighboring grid points depending on the
257 respective distances, keeping H₂O mass conserved. Hence, the next contrail during the same
258 time step interval finds less humidity and is thinner. In this method, the results depend on the
259 sequence of flights. The aircraft which flies first has a thicker contrail than aircraft later in the

260 waypoint input. The accuracy of this approach depends on the ratio of the time step to the
261 contrail life time. The accuracy increases for smaller time step sizes.

262 We note that the coupling between CoCiP and CAM transfers grid cell mean values from
263 CAM to CoCiP and the sum of all contrail sources or sinks within a grid cell back from
264 CoCiP to CAM. As a consequence, the mass of H₂O uptake by a contrail during the time step
265 is spread over the grid cell immediately. Because of the large difference between contrail
266 scales (widths of order 0.1-10 km) and grid scales (about 200 km), humidity variations at
267 contrail scales cannot be resolved. A global model with far higher spatial resolution would be
268 required to overcome this problem.

269 **2.4 Model runs**

270 Three runs were performed with CAM3+/IMPACT/CoCiP for this study, see Table 1. Run 0
271 is the non-coupled (offline) reference case in which CAM runs without aviation emissions
272 while CoCiP is run using nominal aircraft emissions. Here, CoCiP uses the meteorological
273 fields from CAM in the same manner as it used numerical weather prediction results in the
274 past [*Schumann and Graf, 2013*]. Run 1 uses the coupled method (online) and simulates the
275 effects of contrails on the hydrological cycle for nominal aircraft emissions. Run 2 uses
276 aircraft emissions 100 fold increased to enhance the aviation effects beyond climate noise.
277 The results for runs 0 and 1 are from 30 years of simulation after several years of spin-up.
278 Because of limited computing resources, Run 2 includes just one year restarted from run 1
279 files.

280 **3 Results and Discussion**

281 **3.1 CoCiP results**

282 This section describes the contrail results in some detail to explain the physics simulated and
283 to compare with observations. Some annual and global mean contrail properties for run 0 and
284 1 are given in Table 2. Unless otherwise stated, quantitative results are from run 1. The
285 interannual variability of the 30-year mean values of CoCiP results as listed is small, and run
286 1-0 differences in Table 2 are significant.

287 **3.1.1 Basic contrail properties**

288 *a. Traffic*

289 The emissions included in CAM are derived from 182.2 Tg of annual fuel consumption of
290 which CoCiP analyses 83.2 % (the rest comes from emissions near airports which are added

291 directly into the lower model levels of CAM). The global mean traffic density above 4.5 km
292 altitude is $0.0072 \text{ km} (\text{km}^2 \text{ h})^{-1}$. About 92 % of all flight segments occur in the Northern
293 Hemisphere. Maximum traffic occurs near 40°N over North America ($70\text{-}115^\circ\text{W}$), Europe
294 ($7^\circ\text{W}\text{-}15^\circ\text{E}$), and Asia ($100\text{-}130^\circ\text{E}$).

295 *b. Contrail formation*

296 CoCiP computes the contrail properties for each given aircraft type. The average fuel
297 consumption, mass, speed, and overall propulsion efficiency of contrail forming aircraft are
298 4.60 kg km^{-1} , 116 Mg, 225 m s^{-1} , and 0.31, respectively. The contrail forming aircraft
299 consume slightly more fuel (5.33 kg km^{-1}) than the rest of the fleet. About 15 % of all the
300 flight segments cause contrail formation in the CAM atmosphere. About 7 % occur in ice
301 supersaturated air causing persistent contrails. About 12 % of all fuel is consumed in regions
302 in which contrails form. (About two times larger fractions were computed for ECMWF input
303 with lower RHi_c [Schumann *et al.*, 2011a].) Contrail forming aircraft fly mainly in the
304 troposphere, at 10.9 km mean altitude, at 220.3 K ambient temperature, at 116 % relative
305 humidity over ice (RHi , see Figure 1), with mean ambient wind shear of 0.0023 s^{-1} and Brunt-
306 Väisälä frequency of 0.013 s^{-1} . The computed RHi pdf is similar to observations [Immler *et*
307 *al.*, 2008]. The global mean contrail temperature (-53.1°C) is about 5 to 10 K below the mean
308 threshold temperature for contrail formation, and close to the values of -52°C deduced for
309 contrails over the USA from day and night observations by Bedka *et al.* [2013], and -54.6°C
310 at cloud top deduced by Iwabuchi *et al.* [2012].

311 *c. Contrail properties*

312 CoCiP computes that there are about 3100 contrail segments of 36 km mean length present at
313 a time on average within the CAM atmosphere. A total of 3×10^7 contrail segments are
314 simulated per year. For given shear, stratification, and plume scales, the mean diffusivity
315 values are 14 and $120 \text{ m}^2 \text{ s}^{-1}$ in vertical and horizontal directions. The contrails spread to 8 km
316 mean width and 1 km mean total depth, with large variability. We define two results for the
317 depth. The total depth describes the vertical variance of contrail properties in the Gaussian
318 plume model; the effective depth is the ratio of cross-section area to contrail width
319 [Schumann, 2012]. The latter is smaller because shear causes a horizontally inclined and
320 elongated cross-section.

321 The aircraft emit on average $5.3 \times 10^{12} \text{ m}^{-1}$ soot particles per flight distance. The contrails
322 contain about $3 \times 10^{12} \text{ m}^{-1}$ of ice particles per flight distance. Hence, about 56 % of the ice
323 particles survive wake, aggregation, and turbulent losses in the model. The ice water content

324 (IWC) in contrails (and cirrus) correlates with ambient temperature and ambient relative
325 humidity [Schiller *et al.*, 2008]. Figure 2 compares the pdf of computed IWC with the
326 approximate $IWC/(mg\ m^{-3}) = \exp(6.97 + 0.103\ T/^\circ C)$ [Schumann, 2002]. This
327 parameterization was used, e.g., by Chen and Gettelman [2013] to compute the contrail IWC;
328 it gives reasonable estimates for the mean but underestimates IWC variability.

329 On average, the IWC in contrails is found to be equivalent to an amount of water vapor at
330 relative humidity over ice of about 15 %. This value is consistent with the mean RH_i in the
331 ambient air. A growing contrail may contain less ice water and a shrinking contrail more ice
332 water than this mean value. Hence, as shown in Figure 1, long-lived contrails also exist in
333 subsaturated air, as observed [Kübbeler *et al.*, 2011; Iwabuchi *et al.*, 2012; Kaufmann *et al.*,
334 2014].

335 The total mean and median values of contrail properties per unit length vary over several
336 orders of magnitude; see Table 3. The values are averages over all contrail segments without
337 accounting for contrail overlap. The median values are smaller than the mean values which
338 are controlled by a few very thick old contrails. The ice mass per flight distance values (6-50
339 kg/m) is of a magnitude similar to LES results [Unterstrasser and Gierens, 2010b; Lewellen,
340 2014]. The integral numbers of Table 3 can be used to compute global mean contrail air
341 density, ice water content, ice particle size, optical depth, geometrical depth, extinction
342 coefficient etc. For example, the ratio of volume per distance divided by the mean width (area
343 per distance) defines an effective contrail depth (mean ~800 m, median ~400 m, ½-h-mean
344 145 m). The ratio of ice water mass to emission water mass is about 180 for young (age < 0.5
345 h) contrails, 1800 in the median, and $\sim 1.8 \times 10^6$ in the mean of these simulations. The ratio is
346 close to one in the wake vortex phase [Vay *et al.*, 1998] or sublimating contrails. For old
347 contrails in ice supersaturated air, the ratio may be far larger than found by Knollenberg
348 [1972], who measured in a contrail 18 min after generation. The maximum values are limited
349 by the number and mass of the largest ice particles relative to the mass of H₂O emissions.

350 Because of nearly constant ice number per flight distance but variable plume cross-section,
351 the volume concentration n_{ice} varies from more than $100\ cm^{-3}$ in young contrails to less than 1
352 L^{-1} in aged contrails, see Figure 2. The mean value depends strongly on how the average is
353 defined. When averaging linearly over all contrail segments (many stay narrow), we obtain a
354 high mean value of n_{ice} of $86\ cm^{-3}$. When counting all contrail ice particles globally and
355 dividing by the total volume (segment length \times cross-section area) of all contrail segments,

356 we find that the volume is huge and dominated by the wide old contrails. Hence, this mean
357 value of n_{ice} is far smaller (0.4 cm^{-3}).

358 The mean volume radius varies over a large range, from about half a micrometer to half a
359 millimeter, see Figure 2. The lower bound results from the water mass and the number of soot
360 particles nucleating ice in fresh contrails. The upper size limit is determined by sedimentation.
361 The fall speed reaches values of order 0.5 m s^{-1} for particle radii exceeding $100 \text{ }\mu\text{m}$; the
362 average fall speed is 0.0026 m s^{-1} . Particles sedimenting in supersaturated air may grow
363 quickly. The linear arithmetic mean particle radius r_{vol} is $14 \text{ }\mu\text{m}$. The median value of r_{vol} is
364 smaller ($9 \text{ }\mu\text{m}$). These sizes are representative for young and narrow contrails. Alternatively,
365 we compute a volume mean radius of the ensemble of all contrails from the total contrail ice
366 volume divided by the total number of contrail ice particles, and likewise an effective radius
367 from the ratio of total vertically projected particle cross-section area divided by total particle
368 volume, following common definitions, [McFarquhar and Heymsfield, 1998]. This results in
369 far larger integral mean sizes: $r_{\text{vol}}=27 \text{ }\mu\text{m}$ and $r_{\text{eff}}=35 \text{ }\mu\text{m}$. These large integral values are
370 dominated by the aged contrails with largest volume.

371 These particle sizes appear far larger than usually assumed for linear contrails. *Bedka et al.*
372 [2013] found an average particle effective radius of $9 \text{ }\mu\text{m}$ in MODIS satellite data. Larger
373 mean particle sizes have been observed for contrail cirrus, $20\text{-}25 \text{ }\mu\text{m}$ [Minnis et al., 2013].
374 The remote sensing methods may underestimate the particle sizes because the largest particles
375 may have fallen (e.g., in fall streaks) below a level visible to remote sensing from space.

376 The optical depth τ of contrails may be computed locally as a function of the particle cross-
377 section πr_{area}^2 (with $r_{\text{area}}^2 = r_{\text{vol}}^3/r_{\text{eff}}$ [Schumann et al., 2011b]), volume specific number
378 concentration n_{ice} , and the effective geometrical depth of the contrail plume. For various
379 contrail segments, τ varies strongly; see Figure 2; τ is large for young contrails because of
380 many ice particles grown by uptake of ambient humidity in narrow plumes with large depths.
381 This can be seen from observations and models [Voigt et al., 2011; Jeßberger et al., 2013].
382 Later, τ may grow in rising air masses with increasing humidity but generally decreases and
383 approaches zero while the contrails spread laterally and finally sublimate. The pdf of $\log \tau$ has
384 a negative skewness: a few contrails get thick while most have small τ ; some are subvisible.
385 The same type of asymmetry in the pdf of $\log \tau$ has been simulated by *Kärcher and Burkhardt*
386 [2013] for contrails and measured by *Immler et al.* [2008] for contrail-cirrus. The global mean
387 optical depth τ is 0.29, which is close to observed values [Voigt et al., 2011]. The global mean

388 value is slightly larger than the value for linear contrails derived by *Bedka et al.* [2013] from
389 MODIS (0.19-0.26). Contrails detected with an Automatic Contrail Tracking Algorithm
390 (ACTA) from Meteosat observations by *Vázquez-Navarro et al.* [2015] have very similar
391 optical thickness, mean: 0.34, median: 0.24.

392 The RF induced by contrail segments varies strongly, see Figure 3. In rough agreement with
393 observations [*Vázquez-Navarro et al.*, 2015], individual contrail segments may cause local RF
394 values per contrail area (segment width \times length) exceeding 60 W m^{-2} , with mean values of
395 order 10 W m^{-2} . The frequent zero SW RF values result from nighttime contrails. The local
396 net RF may be positive or negative and far larger than the mean value. *Vázquez-Navarro et al.*
397 [2015] found larger mean values because their method mainly detects geometrically and
398 optically thick contrails. The shape of the SW and LW RF pdf's is similar to theory
399 predictions [*Kärcher and Burkhardt*, 2013], but negative RF values were not expected in that
400 study.

401 The age of the simulated contrails varies between a few minutes and 36 h. The mean age is
402 computed as the arithmetic mean of all contrail segment ages. The computed mean contrail
403 age is about 2 h. The contrail ages tend to increase for decreasing ambient humidity (run 1
404 compared to run 0) because of reduced sedimentation for lower humidity. The upper limit of
405 36 h is reached only 18 times globally in 30-years simulations. Ages of individual contrails
406 exceeding 10 h occur rarely, see Figure 4 (the pdf is generated from a 3 % subsample of 1-
407 year simulation data, hence, misses the few contrails with the upper limit age of 36 h). The
408 lifetimes are within the range of results derived with ACTA from Meteosat contrail
409 observations by *Vázquez-Navarro et al.* [2015].

410 The lifetimes depend among other things on vertical motions in the ambient air. In the model,
411 the contrails experience larger mean uplift (100 m) than subsidence (74 m). Plume-spreading
412 in ambient ice supersaturated air causes ice particle growth, because the same ice particles
413 share in a growing amount of humidity. Sinking air warms adiabatically so that contrails
414 sublimate. Rising air tends to increase relative humidity. Strong adiabatic uplift may cause
415 strong growth of the ice particles so that they may start sedimenting and precipitate in fall
416 streaks. Hence, quickly rising contrails may have shorter lifetimes than slowly rising ones. All
417 these properties are consistent with findings from LES and observations [*Iwabuchi et al.*,
418 2012; *Lewellen*, 2014].

419 *d. Comparison with a theoretical concept for sedimentation influence on optical depth*

420 An important metric for contrail radiative properties as a whole, independent of the definition
 421 of contrail width W or contrail depth D , is the total projected surface area S of all contrail ice
 422 particles per unit contrail length, $S = N_{\text{ice}} \pi r_{\text{area}}^2$, where N_{ice} is the number of ice particles per
 423 contrail length and πr_{area}^2 is the mean effective projected cross-section of the ice particles
 424 [Schumann *et al.*, 2011b; Lewellen *et al.*, 2014; Lewellen, 2014]. (Mean values are listed in
 425 Table 3.) The importance of S can be seen from the fact that the optical depth τ of contrails is
 426 $\tau = Q_{\text{ext}} S/W$, where Q_{ext} is the mean extinction efficiency and W the effective width of the
 427 contrail. The product $W\tau = Q_{\text{ext}} S$ is known as total extinction and is important for radiative
 428 forcing of a contrail at a time [Unterstrasser and Gierens, 2010b]. Hence, τ does depend on
 429 the width W and its definition, but W cancels when computing the global radiative forcing
 430 RF, which is the sum of all contrail segment RF values weighted with contrail length and
 431 width divided by the Earth surface. The value of S versus contrail age is plotted in Figure 5.
 432 We see S increasing with contrail age for the first 2 hours and then approaching a constant
 433 which is about 10^2 to $10^4 \text{ m}^2 \text{ m}^{-1}$ in these simulations. S decreases for aged contrails in spite of
 434 increasing contrail width. The magnitude of $Q_{\text{ext}} S$ agrees with observations [Vázquez-
 435 Navarro *et al.*, 2015]. The initial growth comes from particle growth in ice supersaturated air.
 436 Later values are limited because large particles sediment quickly [Schumann, 1996]. Lewellen
 437 [2014] noted the importance of the integral $\int S(t)dt$ over the contrail life-time as a measure for
 438 the total climate impact of the contrail. This integral has similarities with the energy forcing
 439 which we discussed elsewhere [Schumann *et al.*, 2012a]. Since we did not save the integral
 440 value in our simulations, we approximate the integral by $S t_{\text{age}}/2$. The results show that $\int S dt$
 441 approaches asymptotic values of order 10^8 m s for old contrails. The values are close to those
 442 reported by Lewellen [2014] from LES of contrails with particle-size resolving microphysics.
 443 He showed that the integral S relates to fall speed and the sedimentation depth Δz_{sed} by $\int S dt$
 444 $\cong \alpha N_{\text{ice}} \Delta z_{\text{sed}}$, where $\alpha = 18 \pi \eta / (g \rho_{\text{ice}})$ is a parameter resulting from the Stokes law for the
 445 particle terminal fall velocity ($\eta \cong 14 \times 10^{-6} \text{ kg m}^{-1} \text{ s}^{-1}$ is the dynamic viscosity of air, $\rho_{\text{ice}} \cong 917$
 446 kg m^{-3} is the bulk density of ice, $g =$ gravity). The sedimentation depth Δz_{sed} was computed
 447 within CoCiP for each contrail segment. Figure 5 shows that the CoCiP results are roughly
 448 consistent with the theory. The results illustrate the important link between the optical
 449 properties of contrails and ice particle sedimentation in ice supersaturated air. The scatter
 450 around the mean 1:1 correlation indicates that the effective S values depend also on other
 451 parameters: Lewellen [2014] noted the importance of the depth of the ice supersaturated layer
 452 below flight levels. In addition, we have non-steady and spatially variable meteorology, and

453 size-dependent fall speeds differing from the Stokes law. We see that the essential physics of
454 contrail optical depth formation as simulated by CoCiP is similar to LES results.

455 *e. Comparison of contrail properties with observations from space*

456 In addition to the comparisons mentioned, we compare the computed contrail properties with
457 satellite observations. *Iwabuchi et al.* [2012] used satellite pictures (MODIS) to identify linear
458 contrails and derived their altitude and thickness from collocated space lidar (CALIPSO)
459 observations. The method was applied for the domain 15-85°N and 180°W - 80°E, see Figure
460 6. Contrails were detected mainly over the North Atlantic. Although we find a larger share of
461 contrails over the continents, the vertical distribution of the contrails versus latitude in the
462 model is similar to that observed, see Figure 7. Some of the simulated (and observed)
463 contrails at low latitudes rise above 14 km altitude, above the maximum flight levels where
464 contrails form (13.1 km). This is a consequence of rising air masses as occurring in the tropics
465 over continents [*Pauluis et al.*, 2008]. The computed mean contrail altitude (10.5 ± 1.2 km) is
466 slightly lower than observed (10.9 ± 1 km). Some of the low-level contrails may result over
467 continents from aircraft during ascent or descent. Others may occur below thick high-level
468 clouds and be missed by lidar observations.

469 Figure 8 shows that the pdf of optical depth from CoCiP is close to that derived from MODIS
470 and CALIPSO. The differences between the model results for run 1 and 0 are significant but
471 comparable to the differences between the measurements in the two years (with slightly
472 different lidar properties [*Iwabuchi et al.*, 2012]). Figure 9 compares the computed and
473 observed width and vertical geometrical depth of contrails. We note the large scatter of the
474 data. Perhaps, CoCiP slightly overestimates the total depth. The effective depth appears to fit
475 the observations better. The contrail width pdf (not shown) is a maximum at zero width and
476 decreases exponentially with 5 km median and 8.1 km mean width. The width range of ACTA
477 contrails is more limited (7.8 ± 2 km) [*Vázquez-Navarro et al.*, 2015].

478 Figure 10 compares the difference in the diurnal cycle of cirrus cover and outgoing longwave
479 radiation (OLR) between the North Atlantic region (NAR, 45°-55°N, 10°-45°W), and a
480 corresponding South Atlantic Region (SAR, 45°-55°S, 10°-45°W) from the model with
481 results from 8 years of satellite observations. Cirrus cloud cover [*Ewald et al.*, 2013] and
482 outgoing longwave radiation [*Vázquez-Navarro et al.*, 2013] data were derived from Meteosat
483 Second Generation (MSG) infrared satellite observations. The anomalies have zero mean
484 values. Air traffic density in the SAR is practically zero while traffic in the NAR shows a
485 systematic double-wave diurnal cycle [*Graf et al.*, 2012]. Anomalies of cirrus cloud cover and

486 OLR differences between NAR and SAR from MSG show similar patterns with 2-4 h delay.
487 This “aviation fingerprint” was used to quantify aviation induced cirrus changes [*Graf et al.*,
488 2012; *Schumann and Graf*, 2013]. The delay can be interpreted as the time it takes to let ice
489 particles grow (see Figure 5) and spread from fresh contrails to extended cirrus cover. The
490 results suggest that contrail cirrus contribute about 2 % of cirrus cover and about 1 W m^{-2} of
491 radiative forcing in this region. The diurnal cycle from the sum of CoCiP contrail cover and
492 CAM cirrus cover and corresponding longwave radiances is consistent in shape and amplitude
493 with the MSG results. They agree approximately also with results from the offline CoCiP-
494 ECMWF combination in *Schumann and Graf* [2013].

495 Also, the interannual variability of the MSG results is comparable in magnitude to the
496 variability in the CoCiP results. This suggests that CoCiP simulates most of the processes
497 controlling this contrail cirrus signal. The ratio of regional LW RF to global LW RF (see
498 Table 2) is 6.12 and 6.13 in runs 0 and 1, respectively. The ratio was 5.71 in the previous
499 study with ECMWF meteorology. This ratio was used to extrapolate the regional LW RF to
500 the global RF. Hence, the coupling does not change the main conclusions from earlier CoCiP
501 studies.

502 We looked for a local response of cirrus cover and OLR to dehydration following the diurnal
503 traffic cycle. The results from CAM do not reflect such a diurnal cycle. Different time scales
504 of contrail cirrus and dehydration effects would be important when discussing mitigation
505 options. Also *Chen and Gettelman* [2013] computed a far smaller amplitude of a double-wave
506 diurnal cycle in global model results of LW RF for this region than observed. Hence, the
507 dehydration effects of the contrails within CAM are either slow or not large enough to excite
508 a semi-diurnal cycle. Note that most contrails are thinner than 1 km. Perhaps the coarse CAM
509 grid cells (about $1 \text{ km} \times 180 \text{ km} \times 220 \text{ km}$) smooth out any local response of cirrus to
510 dehydration.

511 *f. Some global contrail properties*

512 Figure 11 shows the annual mean global cirrus and contrail cover. The mean cirrus cover
513 computed in these simulations in CAM is 40 % ~~–~~ The value of cloud cover depends critically on the
514 method used, and is specified here as a function of assumed probability density function of
515 supersaturation within each grid (Wang and Penner, 2010). The result is roughly consistent with a
516 range of satellite observations of thin and opaque high-level clouds ~~consistent with observations~~
517 [*Stubenrauch et al.*, 2013]. The mean contrail cover with optical depth $\tau > 0.1$ is nearly 100
518 times smaller: 0.50 %. Maximum values of up to 12 % are computed for high-traffic regions

519 in North America and Europe. The mean product width \times length \times τ of all individual contrail
520 segments divided by the Earth surface area is 0.29 %.

521 The global contrail cover estimated in early assessments was below 0.1% [*Sausen et al.*, 1998;
522 *Penner et al.*, 1999]. The computed contrail cover is about 5 times larger than derived from
523 linear contrails in satellite data [*Palikonda et al.*, 2005; *Meyer et al.*, 2007]. More recent
524 observation results are larger [*Minnis et al.*, 2013]. *Burkhardt and Kärcher* [2009] and
525 *Frömming et al.* [2011] show that the computed contrail cover depends strongly on the
526 assumed threshold value of optical depth used to discriminate contrails from clear sky. *Rap et al.*
527 *al.* [2010b] estimated the global mean annual linear contrail coverage for air traffic of the year
528 2002 to be approximately 0.11 %. *Burkhardt and Kärcher* [2011] reported a contrail cirrus
529 cover for year 2002 of about 0.23 %. *Schumann and Graf* [2013] for year 2006 computed a
530 global mean cover of 0.23 %. The differences of the present study from previous results using
531 CoCiP come mainly from the larger soot number emission index (10^{15} kg⁻¹ instead of
532 $\sim 3.5 \times 10^{14}$ kg⁻¹). For a factor 2 increase of the soot emission index, we computed increases of
533 visible contrail cover by 1.29, contrail age by 1.16, contrail width by 1.22, contrail
534 geometrical depth by 1.14, and net contrail RF of 1.64 [*Schumann et al.*, 2013].

535 As described above, we compute contrail RF defined by the difference in net incoming
536 radiative fluxes at top of the atmosphere with and without contrails. The longwave (LW) part
537 of this RF is always positive and warming, the shortwave (SW) part is negative and cooling,
538 the net effect (sum of LW and SW RF) is often small compared to the LW forcing, and may
539 be positive or negative locally. The global RF distribution is shown in Figure 12. The net RF
540 reaches maximum values of more than 1 W m⁻² locally over North America and Europe. The
541 mean values are 0.584 ± 0.045 W m⁻² over mid Europe (10°W-20°E, 40°N-55°N) and
542 0.410 ± 0.018 W m⁻² over continental USA (65°W-130°W, 25°N-55°N). For run 1, CoCiP
543 computes a global mean net RF of 0.063 W m⁻² (LW: 0.14 W m⁻², SW: -0.08 W m⁻²). The
544 annual mean net RF is positive everywhere on the globe. The global mean LW RF value is 12
545 % larger than computed by CoCiP with ECMWF data [*Schumann and Graf*, 2013], mainly
546 because of the larger soot emission index.

547 The computed RF values are far larger than those estimated previously for linear contrails
548 [*Minnis et al.*, 1999; *Rap et al.*, 2010b; *Frömming et al.*, 2011; *Yi et al.*, 2012; *Chen and*
549 *Gottelman*, 2013; *Spangenberg et al.*, 2013], 5 times larger than the value estimated for
550 contrail cirrus for the same traffic by *Chen and Gottelman* [2013], and nearly double the value

551 estimated with a global contrail cirrus model for traffic of the year 2002 by *Burkhardt and*
552 *Kärcher* [2011].

553 As indicated, some of the comparisons point to possible overestimates of contrail cover and
554 optical thickness by CoCiP. This would imply overestimates of SW and LW RF. As in
555 previous CoCiP studies, the magnitude of the computed SW/LW ratio is quite large (0.56).
556 This SW/LW ratio varies between 0.2 and 0.8 in the literature [*Haywood et al.*, 2009; *Myhre*
557 *et al.*, 2009; *Yi et al.*, 2012; *Minnis et al.*, 2013; *Schumann and Graf*, 2013; *Vázquez-Navarro*
558 *et al.*, 2015]. The ratio may get even larger for small ice particles and higher contrail
559 temperatures [*Meerkötter et al.*, 1999; *Zhang et al.*, 1999]. For fixed LW RF, a smaller
560 SW/LW ratio would imply a larger net RF value. Besides on contrail life times and diurnal
561 variations. Moreover, the RF values depend on the radiances without contrails, cloud
562 temperatures, ice water path, optical ice particle properties, cloud overlap, and 3-D effects
563 [*Meerkötter et al.*, 1999; *Markowicz and Witek*, 2011; *De Leon et al.*, 2012; *Forster et al.*,
564 2012; *Yi et al.*, 2012]. Hence, the net RF may be both larger and smaller than 0.06 W m^{-2} .

Formatiert: Schriftart: 12 Pt.

Formatiert: Schriftart: 12 Pt.

Formatiert: Schriftart: 12 Pt., Kursiv

Formatiert: Schriftart: 12 Pt.

565 Correct modelling of the optical properties may be more important than correct modelling of
566 humidity exchange. Note that the reported net RF includes only the contrail effects.
567 Contributions from dehydration in CAM are discussed below.

568 3.1.2 Impact of changed background meteorology on contrail properties

569 Figure 13 depicts the annual and zonal mean emissions of water from aircraft engines into the
570 atmosphere, either directly (EA) or into contrails (EC). The figure also depicts the water
571 released from contrails, CA. As explained above, the contrails take water from engine
572 emissions and from background humidity in ice-supersaturated air masses (negative CA) and
573 release water when sublimating in subsaturated air (positive CA). Since the amount of H₂O
574 taken from ambient air is far larger than the emission, we find negative “emissions” in the CA
575 field of H₂O at flight levels, and large positive values further down. The negative CA at flight
576 levels in the upper troposphere implies dehydration and the positive CA lower down implies
577 hydration contributions. For steady climate, the annual mean of CA becomes equal to EC, the
578 amount of H₂O entering young contrails. Here the total budget is the result of the uptake of
579 water by contrail minus the release and these exchanges are far larger than the net emissions.

580 The H₂O mass inventory in contrails amounts to 32 Tg for run 1, which is large; it
581 corresponds to 14 % of the annual aviation H₂O mass emissions. The young contrails (age <
582 0.5 h) contain 2.5 % of this mass (Table 3). The total ice mass content in all young contrails at
583 a given time is $7.4 \times 10^8 \text{ kg}$. *Chen and Gettelman* [2013] estimated this to be about $1 \times 10^7 \text{ kg}$;

584 the large difference may explain different RF values. The mean emission altitude from
585 engines into atmosphere z is derived from an integral $z_{EC} = \int z \, dm / \int dm$, where dm is the local
586 EC mass contribution. The value z_{EC} defines a mean contrail formation altitude. This altitude
587 is 10.9 km in run 1. The corresponding altitude of water release to the atmosphere z_{CA} is 700
588 m lower. For a mean contrail age of 2 h, this corresponds to a mean fall speed of 0.1 m s^{-1} ,
589 which appears reasonable for the particle sizes computed. Perhaps the fall time has to be
590 added to the time of contrail formation and spreading to obtain the time scale of cirrus
591 changes, so that the total time-scale may reach half a day. This may further explain why the
592 semi-diurnal cycle in the NAR does not show up in the CAM results in Figure 10.

593 Contrail formation reduces ambient humidity locally (Figure 1) with the consequence of
594 getting fewer or thinner contrails (Figure 2), which are slightly longer living (Figure 43).
595 Contrail ice particle sedimentation brings humidity to lower levels. Even without
596 sedimentation, contrails in subsiding air sublimate at lower levels. Contrails in rising air
597 masses occur often because relative humidity increases from adiabatic cooling. Hence, some
598 hydration occurs at higher levels but does not show up in the longitudinal mean values.

599 The effect of humidity exchange on contrails and the background atmosphere can be
600 quantified by comparing mean results of runs 0 and 1, see Table 2. The contrails in the
601 coupled model run 1 have 5 % more ice particles, but 29 % less ice water content, and 23 %
602 smaller effective radius than in run 0. The total H_2O mass inventory changes by 39 %. So the
603 coupling effect is important. The contrails have 14 % lower optical depth and 5 % larger age.
604 They live longer because the smaller ice particles sediment more slowly. The change in the
605 net radiative forcing, from ~ 0.07 to $\sim 0.06 \text{ W m}^{-2}$, is comparably small, about 14 %.

606 3. 2 CAM Results

607 3.2.1 Normal Traffic Emissions

608 The redistribution of water by contrails in the atmosphere should have strongest effects on
609 humidity in the background atmosphere at northern mid-latitudes, where most contrails form.
610 For normal traffic, the CAM results show only small changes. The run 1 – 0 differences are
611 small compared to the interannual variability in the atmosphere, see Figure 14. In order to
612 understand this, we estimate the order of magnitude of the source rate required to cause an
613 appreciable change in background humidity. A background humidity mass concentration of
614 order 100 ppm and a life time of order 10 days (a 1 month life time cannot be excluded
615 [Forster *et al.*, 2003]) corresponds to a background humidity source of order $100 \text{ ppm}/10 \text{ d} \cong$

616 10^{-10} s^{-1} or 3×10^{-4} /month. In the zonal and annual mean (Figure 12), the source rates from
617 contrail sublimation (CA) amounts to $10^{-5} \text{ month}^{-1}$ at maximum. Hence, the humidity
618 contributions from contrails are more than a factor of 30 smaller in magnitude than natural
619 water sources, apparently too small to be visible in 30-year climate mean values.

620 Radiative forcing should respond strongly to humidity and cloud changes in the troposphere
621 and the lower stratosphere [Chen *et al.*, 2000; Riese *et al.*, 2012]. Figure 15 shows the RF
622 computed from the difference in run 1-run 0. The interannual RF standard deviations are 0.2-
623 0.3 W m^{-2} . The interannual changes are smaller than the variability of top-of-the atmosphere
624 radiances derived from satellites and from atmospheric-ocean climate models [Kato, 2009;
625 Stephens *et al.*, 2015] and similar to the variability in CAM5 [Zhou and Penner, 2014], but far
626 larger than the variability ($<0.1 \text{ W m}^{-2}$) of nudged models [Chen and Gettelman, 2013].

627 Assuming N-2 independent results from N=30 years of simulations, the standard error is $\sqrt{28}$
628 smaller, about 0.05 W m^{-2} . Hence, the mean LW RF is practically zero, and the SW and net
629 RF values are mostly positive, but only weakly significant. A positive net RF could not be
630 explained with reduced cirrus clouds [Burkhardt and Kärcher, 2011].

631 The annual mean RF values vary from year to year and show significant correlations with
632 other annual and global mean diagnostics from CAM. Figure 16 shows strong correlations of
633 RF with liquid water path and with low-level cloud cover. For SW RF, the correlation with
634 low cloud cover is stronger than with high-level cloud cover. Hence, the interannual variability
635 in RF appears to be linked mainly to the variability in low-level cloudiness.

636 **3.2.2 Enhanced Traffic Emissions**

637 In order to increase the signal-to-noise ratio in the CAM simulations, we consider run 2 with
638 100 times enhanced traffic emissions. The increased traffic emissions are implemented in
639 CoCiP using the same number of flights but 100 times larger fuel consumption, implying 100
640 times larger water mass and soot number emissions. This causes large changes in the contrail
641 properties, see Table 4. We see 94 times larger number of ice particles per unit length, and 6
642 times larger ice particle number volume concentration, but 60 % less specific ice water
643 content. Hence, as expected, e.g., from Unterstrasser and Gierens [2010a], the increased soot
644 emission causes far more contrail ice particles while the enhanced water emissions are less
645 important. Moreover, CoCiP computes doubled mean contrail life time, 4 times larger optical
646 depth, 8 times more contrail cover, and about 14 times larger net contrail RF.

647 CAM does not see the soot but sees changes in water emissions CA (with a small contribution
648 from EA). CoCiP computes about ten times larger contrail ice water mass inventory, and
649 about the same sedimentation depth. Figure 13 (lower panels) shows the distributions of the
650 effective emissions CA for runs 1 and 2. We find similar distributions with about 10 times
651 larger CA values in run 2. The ratios of the maximum, minimum, and global mean rms values
652 of CA in runs 2 and 1 are 12.4, 9.8 and 12.9, respectively. Hence, the water inventory and the
653 exchange between contrails and background atmosphere in run 2 is about ten times larger than
654 in run 1.

655 Figure 14 shows that the mean humidity profile responds to the changed water exchange
656 significantly. The contrails cause a global dehydration mainly of the tropopause region
657 (including the lower stratosphere) and a local increase of humidity in the mid troposphere
658 below the main flight levels at Northern mid-latitudes. The global mean humidity is
659 decreasing. Hence, the redistribution of humidity by contrails changes the entire hydrological
660 cycle.

661 Figure 17 plots the RF of dehydration derived by CAM from run 1 - 0 differences as a
662 function of contrail ice water inventory, which is used as a measure for the change in water
663 exchange CA. The mean values are compared in Table 5. For run 2, the RF values are
664 computed from one-year mean of run 2 and 30 annual mean values of run 0. The standard
665 deviation from 30 years of run 2 might be a factor of $\sqrt{2}$ larger.

666 The mean SW and LW RF results are significant at the 95 % level for enhanced fuel
667 consumption. SW RF is positive in this case, suggesting that dehydration reduces cloud cover,
668 both in the upper and lower atmosphere, causing lower Earth albedo and, hence, warming the
669 atmosphere. LW RF is negative (cooling), which would be consistent with reduced cloud
670 cover and reduced water vapor in the cold tropopause region. The net RF values are small and
671 have different signs in runs 1 and 2.

672 Table 5 shows that dehydration by contrails causes significant changes of CAM mean values
673 for enhanced emissions. We find reduced cloud cover and reduced water path in all phases.
674 All of these changes are consistent with a causal impact of humidity redistribution by
675 contrails on the hydrological cycle. The results suggest that ice particles sedimenting from
676 contrails transport humidity downwards causing low-level cloud changes. The added humidity
677 at lower levels may enhance liquid water content and cloud droplet sizes and, hence,
678 precipitation. The available diagnostics do not allow us to decide whether the Wegener-

679 Findeisen-Bergeron process acts and contributes to ice particle growth from evaporating cloud
680 droplets, thereby enhancing precipitation.

681 Low-level cloud changes by aviation aerosol have been found before [*Righi et al.*, 2013], but
682 such effects from dehydration have not been reported before. The SW plus LW clear sky RF
683 (see Table 5), mainly from reduced water vapor path, is of opposite sign and far larger in
684 magnitude than the RF from aviation water emissions without contrail formation (about 0.001
685 $W m^{-2}$, [*Wilcox et al.*, 2012]), even when scaling the run 2 values by factors 10 to 100.

686 Interpolating linearly in the ice mass inventories (Figure 17) suggests that the magnitudes of
687 the SW and LW RF components of the dehydration effects for nominal traffic are about 0.04
688 $W m^{-2}$. Because of the different signs of the SW and LW contributions, the net RF from
689 dehydration is smaller, and not much different from the $-0.007 W m^{-2}$ result estimated by
690 *Burkhardt and Kärcher* [2011]. Hence, the dehydration may reduce the RF from contrails, but
691 slightly. Our best estimate for the total net RF stays within the range 0.04-0.08 $W m^{-2}$
692 estimated earlier [*Schumann and Graf*, 2013].

693

694 **4 Conclusions**

695 This paper studied the effects of contrails from aviation on the redistribution of humidity in
696 the atmosphere. For this purpose, we coupled the contrail model CoCiP with the climate
697 model CAM3+/IMPACT (CAM). The contrail model simulates all the individual contrails
698 forming from global air traffic for meteorological conditions as defined by the climate model.
699 The climate model simulates aerosol-cloud processes in the global atmosphere. The coupled
700 model simulates the exchange of humidity between background atmosphere and contrails and
701 the resultant changes in the atmosphere, including cloudiness and the atmospheric part of the
702 hydrological cycle. The results are from two major model runs with and without contrail
703 water exchange, running hourly over 30 years. In addition, the coupled model was run with
704 enhanced air traffic emissions for one year.

705 The major findings are as follows:

- 706 • The mean contrail ensemble properties are as expected from present understanding
707 and consistent with available observations.
- 708 • The computed optical depth values are close to those observed by lidar and satellites
709 from space.
- 710 • In agreement with previous studies, the optical properties of the contrails are strongly
711 linked to ice particle sedimentation in ice supersaturated air.
- 712 • In the coupled model, contrail water content may be 10^3 to 10^6 times larger than the
713 amount of H_2O emitted. About 3000 contrail segments are active at any time on average.
- 714 • Contrail growth causes dehydration at flight levels, the large ice particles sediment, on
715 average by 700 m, eventually sublimate and hydrate the atmosphere at lower levels. In rising
716 air masses, hydration occurs locally at higher levels.
- 717 • The drying at flight levels changes mean contrail properties by +5 to -30 %: Contrails
718 become thinner and with larger mean age. Net contrail RF is reduced by ~15 % from ~0.07 to
719 $\sim 0.06 \text{ W m}^{-2}$.
- 720 • The model simulates a diurnal cycle of cirrus properties in the North Atlantic which
721 reflects the diurnal cycle of air traffic in that region and which is close to that observed by
722 satellites. Dehydration-driven diurnal-cycle cirrus-changes in the global model were not
723 detectable.

724 • The total dehydration RF is too small to be computed for nominal emissions because
725 of climate noise in the freely running atmosphere climate model (interannual RF standard
726 deviations about 0.2 W m^{-2}).

727 • Scaling the fuel consumption by 100 shows significant changes. The contrails respond
728 strongly to the increases in soot emissions causing a larger ice mass inventory in contrails and
729 stronger water exchange between contrails and the background atmosphere. The larger
730 contrail water exchange drives significant mean dehydration effects in the global atmosphere.

731 • Based on these simulations, the redistribution of water by contrails causes negative
732 LW RF because of reduced humidity near the tropopause (opposite sign and far larger than
733 RF from aviation water emissions without contrails) and positive SW from reduced cloud
734 cover, with magnitudes for normal traffic likely less than $\pm 0.04 \text{ W m}^{-2}$. The net dehydration
735 effect is estimated to be about -0.01 W m^{-2} . The sum of contrail and dehydration net RF stays
736 within the range $0.04\text{-}0.08 \text{ W m}^{-2}$ derived for contrail cirrus from earlier studies.

737 • In the global model, dehydration impacts the entire hydrological system, including
738 high and low-level clouds. Both liquid and ice water paths and cloud cover of low and high-
739 level clouds are reduced.

740 The quantitative results are sensitive to model details. For example, the sedimentation is only
741 crudely simulated with CoCiP because the details depend on the particle size spectrum which
742 is not resolved in CoCiP. Possibly, the simulated contrails are slightly thicker than expected
743 from the observations. Thinner contrails would appear, e.g., for a smaller effective soot
744 emission index. As a whole, the comparisons with observations show that the coupled model
745 provides results in reasonable agreement with observations. This is a positive indicator not
746 only for the quality of CoCiP but also the quality of the input fields provided by CAM, in
747 particular with respect to ice supersaturation which is crucial to the prediction of long-lived
748 contrails.

749 This paper discussed the effects of water exchange between contrails and ambient air. Aircraft
750 aerosols from aircraft engines emissions, possibly changed in contrails, may also impact the
751 entire hydrological cycle, and might be studied with an extension of this model in the future.

752

753 **Author contribution.** J.P. and U.S. designed research and wrote the paper. U.S., Y.C., C.Z.,
754 and K.G. coded the programs and data analysis and discussed the results.

755

756 **Acknowledgements.** This research was supported by the Federal Aviation Administration
757 (FAA) within the ACCRI project, and by DLR within the DLR-projects CATS and WeCare.
758 J. E. Penner, Y. Chen and C. Zhou also acknowledge funding from National Science
759 Foundation (NSF). Computing resources (ark:/85065/d7wd3xhc) were provided by the
760 Climate Simulation Laboratory at NCAR's Computational and Information Systems
761 Laboratory, sponsored by the NSF and other agencies.

762

763 **References**

- 764 Atlas, D., Z. Wang, and D. P. Duda (2006), Contrails to cirrus - Morphology, microphysics,
765 and radiative properties, *J. Appl. Meteorol. Clim.*, *45*, 5-19, doi: 10.1175/JAM2325.1.
- 766 Bedka, S. T., P. Minnis, D. P. Duda, T. L. Chee, and R. Palikonda (2013), Properties of linear
767 contrails in the Northern Hemisphere derived from 2006 Aqua MODIS observations,
768 *Geophys. Res. Lett.*, *40*, 772-777, doi:10.1029/2012GL054363.
- 769 Boucher, O., D. Randall, P. Artaxo, C. Bretherton, G. Feingold, P. Forster, V.-M. Kerminen,
770 Y. Kondo, H. Liao, U. Lohmann, P. Rasch, S. K. Satheesh, S. Sherwood, B. Stevens, and
771 X. Y. Zhang (2013), Clouds and Aerosols., in *Climate Change 2013: The Physical Science*
772 *Basis. Contribution of Working Group I to the Fifth Assessment Report of the*
773 *Intergovernmental Panel on Climate Change* edited by T. F. Stocker, et al., pp. 571-657,
774 Cambridge University Press, Cambridge, United Kingdom and New York, NY, USA.
- 775 Brasseur, G. P., R. A. Cox, D. Hauglustaine, I. Isaksen, J. Lelieveld, D. H. Lister, R. Sausen,
776 U. Schumann, A. Wahner, and P. Wiesen (1998), European scientific assessment of the
777 atmospheric effects of aircraft emissions, *Atmos. Env.*, *32*, 2329 - 2418.
- 778 Brasseur, G. P., M. Gupta, B. E. Anderson, S. Balasubramanian, S. Barrett, D. Duda, G.
779 Fleming, P. M. Forster, J. Fuglestedt, A. Gettelman, R. N. Halthore, S. D. Jacob, M. C.
780 Jacobson, A. Khodayari, K.-N. Liou, M. T. Lund, R. C. Miake-Lye, P. Minnis, S. C. Olsen,
781 J. E. Penner, R. Prinn, U. Schumann, H. B. Selkirk, A. Sokolov, N. Unger, P. Wolfe, H.-
782 W. Wong, D. W. Wuebbles, B. Yi, P. Yang, and C. Zhou (2015), Impact of aviation on
783 climate: FAA's Aviation Climate Change Research Initiative (ACCRI) Phase II, *Bull.*
784 *Amer. Meteorol. Soc.*, *in press*, doi: [10.1175/BAMS-D-13-00089.1](https://doi.org/10.1175/BAMS-D-13-00089.1), 2015 *accepted*.
- 785 Burkhardt, U., and B. Kärcher (2009), Process-based simulation of contrail cirrus in a global
786 climate model, *J. Geophys. Res.*, *114*, 1-13, doi:10.1029/2008JD011491.

Formatiert: Schriftart: (Standard)
Times New Roman

787 Burkhardt, U., B. Kärcher, and U. Schumann (2010), Global modelling of the contrail and
788 contrail cirrus climate impact, *Bull. Amer. Meteorol. Soc.*, *91*, 479-484, DOI:
789 10.1175/2009BAMS2656.1.

790 Burkhardt, U., and B. Kärcher (2011), Global radiative forcing from contrail cirrus, *Nature*
791 *Clim. Change*, *1*, 54-58, doi: 10.1038/NCLIMATE1068.

792 Chen, C.-C., and A. Gettelman (2013), Simulated radiative forcing from contrails and contrail
793 cirrus, *Atmos. Chem. Phys.*, *13*, 12525–12536, doi:10.5194/acp-13-12525-2013.

794 Chen, T., W. B. Rossow, and Y. C. Zhang (2000), Radiative effects of cloud-type variations,
795 *J. Clim.*, *13*, 264--286.

796 [De Leon, R. R., Krämer, M., Lee, D. S., and Thelen, J. C. \(2012\), Sensitivity of radiative properties of](#)
797 [persistent contrails to the ice water path, *Atmos. Chem. Phys.*, *12* 7893-7901, doi:10.5194/acp-12-](#)
798 [7893-2012.](#)

799 Ewald, F., L. Bugliaro, H. Mannstein, and B. Mayer (2013), An improved cirrus detection
800 algorithm MeCiDA2 for SEVIRI and its evaluation with MODIS, *Atmos. Meas. Tech.*, *6*,
801 309-322, doi:10.5194/amt-6-309-2013.

802 Fahey, D. W., and U. Schumann (1999), Aviation-Produced Aerosols and Cloudiness, in
803 *Aviation and the Global Atmosphere. A Special Report of IPCC Working Groups I and III*,
804 edited by J. E. Penner, et al., pp. 65-120, Cambridge University Press, New York.

805 Forster, C., A. Stohl, P. James, and V. Thouret (2003), The residence times of aircraft
806 emissions in the stratosphere using a mean emission inventory and emissions along actual
807 flight tracks, *J. Geophys. Res.*, *108*, 8524, doi:10.1029/2002JD002515.

808 Forster, L., C. Emde, S. Unterstrasser, and B. Mayer (2012), Effects of three-dimensional
809 photon transport on the radiative forcing of realistic contrails, *J. Atmos. Sci.*, *69*, 2243-
810 2255, doi: 10.1175/JAS-D-11-0206.1.

811 Frömming, C., M. Ponater, U. Burkhardt, A. Stenke, S. Pechtl, and R. Sausen (2011),
812 Sensitivity of contrail coverage and contrail radiative forcing to selected key parameters,
813 *Atmos. Env.*, *45*, 1483-1490, doi:10.1016/j.atmosenv.2010.11.033.

814 Fueglistaler, S., A. E. Dessler, T. J. Dunkerton, I. Folkins, Q. Fu, and P. W. Mote (2009),
815 Tropical tropopause layer, *Reviews of Geophysics*, *47*, RG1004, DOI:
816 10.1029/2008RG000267.

817 Fusina, F., P. Spichtinger, and U. Lohmann (2007), Impact of ice supersaturated regions and
818 thin cirrus on radiation in the midlatitudes, *J. Geophys. Res.*, *112*, D24S14,
819 doi:10.1029/2007JD008449.

Formatiert: Standard, Leerraum
zwischen asiatischem und westlichem
Text nicht anpassen, Leerraum
zwischen asiatischem Text und Zahlen
nicht anpassen

820 Gettelman, A., and C. Chen (2013), The climate impact of aviation aerosols, *Geophys. Res.*
821 *Lett.*, doi: 10.1002/grl.50520.

822 Graf, K., U. Schumann, H. Mannstein, and B. Mayer (2012), Aviation induced diurnal North
823 Atlantic cirrus cover cycle, *Geophys. Res. Lett.*, *39*, L16804, doi: 10.1029/2012GL052590.

824 Haywood, J. M., R. P. Allan, J. Bornemann, P. M. Forster, P. N. Francis, S. Milton, G. Rädcl,
825 A. Rap, K. P. Shine, and R. Thorpe (2009), A case study of the radiative forcing of
826 persistent contrails evolving into contrail-induced cirrus, *J. Geophys. Res.*, *114*, D24201,
827 doi:10.1029/2009JD012650.

828 Hendricks, J., B. Kärcher, and U. Lohmann (2011), Effects of ice nuclei on cirrus clouds in a
829 global climate model, *J. Geophys. Res.*, *116*, D18206, 10.1029/2010JD015302.

830 Heymsfield, A., D. Baumgardner, P. DeMott, P. Forster, K. Gierens, and B. Kärcher (2010),
831 Contrail microphysics, *Bull. Amer. Meteorol. Soc.*, *90*, 465-472, doi:
832 10.1175/2009BAMS2839.1.

833 Heymsfield, A. J., R. P. Lawson, and G. W. Sachse (1998), Growth of ice crystals in a
834 precipitating contrail, *Geophys. Res. Lett.*, *25*, 1335-1338, DOI: 10.1029/98GL00189.

835 Immler, F., R. Treffeisen, D. Engelbart, K. Krüger, and O. Schrems (2008), Cirrus, contrails,
836 and ice supersaturated regions in high pressure systems at northern mid latitudes, *Atmos.*
837 *Chem. Phys.*, *8*, 1689--1699, doi:10.5194/acp-8-1689-2008.

838 Iwabuchi, H., P. Yang, K. N. Liou, and P. Minnis (2012), Physical and optical properties of
839 persistent contrails: Climatology and interpretation, *J. Geophys. Res.*, *117*, D06215,
840 doi:10.1029/2011JD017020.

841 Jensen, E. J., O. B. Toon, L. Pfister, and H. B. Selkirk (1996), Dehydration of the upper
842 troposphere and lower stratosphere by subvisible cirrus clouds near the tropical tropopause,
843 *Geophys. Res. Lett.*, *23*, 825–828, DOI: 10.1029/96GL00722.

844 Jensen, E. J., A. S. Ackermann, D. E. Stevens, O. B. Toon, and P. Minnis (1998), Spreading
845 and growth of contrails in a sheared environment., *J. Geophys. Res.*, *103*, 13,557-513,567,
846 doi:10.1029/98JD02594.

847 Jeßberger, P., C. Voigt, U. Schumann, I. Sölch, H. Schlager, S. Kaufmann, A. Petzold, D.
848 Schäuble, and J.-F. Gayet (2013), Aircraft type influence on contrail properties, *Atmos.*
849 *Chem. Phys.*, *13*, 11965-11984, DOI: 10.5194/acp-13-11965-2013.

850 Kärcher, B., and U. Burkhardt (2013), Effects of optical depth variability on contrail radiative
851 forcing, *Q. J. R. Meteorol. Soc.*, *139*, 1658-1664, DOI:10.1002/qj.2053.

852 Kato, S. (2009), Interannual variability of the global radiation budget, *J. Clim.*, *22*, 4893-
853 4907, DOI: 10.1175/2009JCLI2795.1.

854 Kaufmann, S., C. Voigt, P. Jeßberger, T. Jurkat, H. Schlager, A. Schwarzenboeck, M.
855 Klingebiel, and T. Thornberry (2014), In-situ measurements of ice saturation in young
856 contrails, *Geophys. Res. Lett.*, *NN*, NN, doi: 10.1002/2013GL058276.

857 Kienast-Sjögren, E., P. Spichtinger, and K. Gierens (2013), Formulation and test of an ice
858 aggregation scheme for two-moment bulk microphysics schemes, *Atmos. Chem. Phys.*, *13*,
859 9021-9037, doi:10.5194/acp-13-9021-2013.

860 Knollenberg, R. G. (1972), Measurements of the growth of the ice budget in a persisting
861 contrail, *J. Atmos. Sci.*, *29*, 1367-1374.

862 Korolev, A., and I. P. Mazin (2003), Supersaturation of water vapor in clouds, *J. Atmos. Sci.*,
863 *60*, 2957--2974.

864 Kübbeler, M., M. Hildebrandt, J. Meyer, C. Schiller, T. Hamburger, T. Jurkat, A. Minikin, A.
865 Petzold, M. Rautenhaus, H. Schlager, U. Schumann, C. Voigt, P. Spichtinger, J.-F. Gayet,
866 C. Gourbeyre, and M. Krämer (2011), Thin and subvisible cirrus and contrails in a
867 subsaturated environment, *Atmos. Chem. Phys.*, *11*, 5853-5865, doi:10.5194/acp-11-5853-
868 2011.

869 Lee, D. S., D. W. Fahey, P. M. Forster, P. J. Newton, R. C. N. Wit, L. L. Lim, B. Owen, and
870 R. Sausen (2009), Aviation and global climate change in the 21st century, *Atmos. Env.*, *43*,
871 3520-3537, doi:10.1016/j.atmosenv.2009.04.024.

872 Lee, D. S., G. Pitari, V. Grewe, K. Gierens, J. E. Penner, A. Petzold, M. J. Prather, U.
873 Schumann, A. Bais, T. Berntsen, D. Iachetti, L. L. Lim, and R. Sausen (2010), Transport
874 impacts on atmosphere and climate: Aviation, *Atmos. Env.*, *44*, 4678-4734,
875 doi:10.1016/j.atmosenv.2009.06.005.

876 Lewellen, D. C., and W. S. Lewellen (2001), The effects of aircraft wake dynamics on
877 contrail development, *J. Atmos. Sci.*, *58*, 390-406.

878 Lewellen, D. C. (2014), Persistent contrails and contrail cirrus. Part II: Full lifetime behavior,
879 *J. Atmos. Sci.*, *71*, 4420-4438, DOI: 10.1175/JAS-D-13-0317.1.

880 Lewellen, D. C., O. Meza, and W. W. Huebsch (2014), Persistent contrails and contrail cirrus.
881 Part I: Large-eddy simulations from inception to demise, *J. Atmos. Sci.*, *70*, 4399-4419,
882 DOI: 10.1175/JAS-D-13-0316.1.

883 Mannstein, H., and U. Schumann (2005), Aircraft induced contrail cirrus over Europe,
884 *Meteorol. Z.*, *14*, 549 - 554, 10.1127/0941-2948/2005/0058.

885 Markowicz, K. M., and M. Witek (2011), Sensitivity study of global contrail radiative forcing
886 due to particle shape, *J. Geophys. Res.*, *116*, D23203, doi:10.1029/2011JD016345.

887 McFarquhar, G. M., and A. J. Heymsfield (1998), The definition and significance of an
888 effective radius for ice clouds, *J. Atmos. Sci.*, *55*, 2039-2052.

889 Meerkötter, R., U. Schumann, P. Minnis, D. R. Doelling, T. Nakajima, and Y. Tsushima
890 (1999), Radiative forcing by contrails, *Ann. Geophysicae*, *17*, 1080-1094, doi:
891 10.1007/s00585-999-1080-7.

892 Meyer, R., R. Buell, C. Leiter, H. Mannstein, S. Pechtl, T. Oki, and P. Wendling (2007),
893 Contrail observations over Southern and Eastern Asia in NOAA/AVHRR data and
894 comparisons to contrail simulations in a GCM, *Int. J. Rem. Sens.*, *28*, 2049-2069,
895 doi:10.1080/01431160600641707.

896 Minnis, P., D. F. Young, D. P. Garber, L. Nguyen, W. L. Smith Jr., and R. Palikonda (1998),
897 Transformation of contrails into cirrus during SUCCESS, *Geophys. Res. Lett.*, *25*, 1157-
898 1160, doi:10.1029/97GL03314.

899 Minnis, P., U. Schumann, D. R. Doelling, K. Gierens, and D. W. Fahey (1999), Global
900 distribution of contrail radiative forcing, *Geophys. Res. Lett.*, *26*, 1853 - 1856, doi:
901 10.1029/1999GL900358.

902 Minnis, P., S. T. Bedka, D. P. Duda, K. M. Bedka, T. Chee, J. K. Ayers, R. Palikonda, D. A.
903 Spangenberg, K. V. Khlopenkov, and R. Boeke (2013), Linear contrail and contrail cirrus
904 properties determined from satellite data, *Geophys. Res. Lett.*, *40*, 3220-3226, doi:
905 10.1002/grl.50569.

906 Murcray, W. B. (1970), On the possibility of weather modification by aircraft contrails, *Mon*
907 *Wea. Rev.*, *98*, 745-748, doi: 10.1175/1520-0493(1970)098<0745:OTPOWM>2.3.CO;2

908 Myhre, G., M. Kvalevag, G. Rädcl, J. Cook, K. P. Shine, H. Clark, F. Karcher, K. Markowicz,
909 A. Karda, O. Wolkenberg, Y. Balkanski, M. Ponater, P. Forster, A. Rap, and R. Rodriguez
910 de Leon (2009), Intercomparison of radiative forcing calculations of stratospheric water
911 vapour and contrails, *Meteorol. Z.*, *18*, 585-596, DOI 10.1127/0941-2948/2009/0411.

912 Naiman, A. D., S. K. Lele, and M. Z. Jacobson (2011), Large eddy simulations of contrail
913 development: Sensitivity to initial and ambient conditions over first twenty minutes, *J.*
914 *Geophys. Res.*, *116*, D21208, doi:10.1029/2011JD015806.

915 Palikonda, R., P. Minnis, D. P. Duda, and H. Mannstein (2005), Contrail coverage derived
916 from 2001 AVHRR data over the continental United States of America and surrounding
917 areas, *Meteorol. Z.*, *14*, 525-536, DOI: 10.1127/0941-2948/2005/0051.

918 Pauluis, O., A. Czaja, and R. Korty (2008), The global atmospheric circulation on moist
919 isentropes, *Science*, *321*, 1075-1078.

920 Penner, J. E., D. H. Lister, D. J. Griggs, D. J. Dokken, and M. McFarland (1999), *Aviation
921 and the global atmosphere – A special report of IPCC working groups I and III.
922 Intergovernmental Panel on Climate Change*, 365 pp., Cambridge University Press.

923 Penner, J. E., Y. Chen, M. Wang, and X. Liu (2009), Possible influence of anthropogenic
924 aerosols on cirrus clouds and anthropogenic forcing, *Atmos. Chem. Phys.*, *9*, 879-896,
925 10.5194/acp-9-879-2009.

926 Ponater, M., S. Marquart, R. Sausen, and U. Schumann (2005), On contrail climate
927 sensitivity, *Geophys. Res. Lett.*, *32*, L10706, 10.1029/2005gl022580.

928 Rap, A., P. M. Forster, J. M. Haywood, A. Jones, and O. Boucher (2010a), Estimating the
929 climate impact of linear contrails using the UK Met Office climate model, *Geophys. Res.
930 Lett.*, *37*, L20703, doi:10.1029/2010GL045161.

931 Rap, A., P. M. Forster, A. Jones, O. Boucher, J. M. Haywood, N. Bellouin, and R. R. D. Leon
932 (2010b), Parameterization of contrails in the UK Met Office Climate Model, *J. Geophys.
933 Res.*, *115*, D10205, doi:10.1029/2009JD012443.

934 Riese, M., F. Ploeger, A. Rap, B. Vogel, P. Konopka, M. Dameris, and P. Forster (2012),
935 Impact of uncertainties in atmospheric mixing on simulated UTLS composition and related
936 radiative effects, *J. Geophys. Res.*, *117*, D16305, doi:10.1029/2012JD017751.

937 Righi, M., J. Hendricks, and R. Sausen (2013), The global impact of the transport sectors on
938 atmospheric aerosol: simulations for year 2000 emissions, *Atmos. Chem. Phys.*, *13*, 9939–
939 9970, doi:10.5194/acp-13-9939-2013.

940 Sausen, R., K. Gierens, M. Ponater, and U. Schumann (1998), A diagnostic study of the
941 global distribution of contrails. Part I: Present day climate, *Theor. Appl. Climat.*, *61*, 127 -
942 141, doi: 10.1007/s007040050058.

943 Sausen, R., I. Isaksen, D. Hauglustaine, V. Grewe, D. S. Lee, G. Myhre, M. O. Köhler, G.
944 Pitari, U. Schumann, F. Stordal, and C. Zerefos (2005), Aviation radiative forcing in 2000:
945 An update on IPCC (1999), *Meteorol. Z.*, *14*, 555 - 561, 10.1127/0941-2948/2005/0049.

946 Schiller, C., M. Krämer, A. Afchine, N. Spelten, and N. Sitnikov (2008), Ice water content of
947 Arctic, midlatitude, and tropical cirrus, *J. Geophys. Res.*, *113*, D24208,
948 doi:10.1029/2008JD010342

949 Schumann, U. (1994), On the effect of emissions from aircraft engines on the state of the
950 atmosphere, *Ann. Geophysicae*, *12*, 365-384.

951 Schumann, U. (1996), On conditions for contrail formation from aircraft exhausts, *Meteorol.*
952 *Z.*, *5*, 4-23.

953 Schumann, U. (2002), Contrail Cirrus, edited by D. K. Lynch, et al., pp. 231-255, Oxford
954 Univ. Press, Oxford.

955 Schumann, U., K. Graf, and H. Mannstein (2011a), Potential to reduce the climate impact of
956 aviation by flight level changes, in *3rd AIAA Atmospheric and Space Environments*
957 *Conference, AIAA paper 2011-3376*, edited, pp. 1-22, Honolulu, Hawaii.

958 Schumann, U., B. Mayer, K. Gierens, S. Unterstrasser, P. Jessberger, A. Petzold, C. Voigt,
959 and J.-F. Gayet (2011b), Effective radius of ice particles in cirrus and contrails, *J. Atmos.*
960 *Sci.*, *68*, 300-321, DOI: 10.1175/2010JAS3562.1.

961 Schumann, U. (2012), A contrail cirrus prediction model, *Geosci. Model Dev.*, *5*, 543–580,
962 doi: 10.5194/gmd-5-543-2012.

963 Schumann, U., K. Graf, H. Mannstein, and B. Mayer (2012a), Contrails: Visible aviation
964 induced climate impact, in *Atmospheric Physics -- Background - Methods - Trends*, edited
965 by U. Schumann, pp. 239-257, Springer, Berlin, Heidelberg, DOI: 10.1007/978-3-642-
966 30183-4_15.

967 Schumann, U., B. Mayer, K. Graf, and H. Mannstein (2012b), A parametric radiative forcing
968 model for contrail cirrus, *J. Appl. Meteorol. Clim.*, *51*, 1391-1406, doi: 10.1175/JAMC-D-
969 11-0242.1.

970 Schumann, U., and K. Graf (2013), Aviation-induced cirrus and radiation changes at diurnal
971 timescales *J. Geophys. Res.*, *118*, 2404-2421, doi: 10.1002/jgrd.50184.

972 Schumann, U., P. Jeßberger, and C. Voigt (2013), Contrail ice particles in aircraft wakes and
973 their climatic importance, *Geophys. Res. Lett.*, *40*, 2867-2872 doi: 10.1002/grl.50539.

974 Spangenberg, P. Minnis, S. T. Bedka, R. Palikonda, D. P. Duda, and F. G. Rose (2013),
975 Contrail radiative forcing over the Northern Hemisphere from 2006 Aqua MODIS data,
976 *Geophys. Res. Lett.*, *40*, 595-600, doi: 10.1002/grl.50168.

977 Spichtinger, P., and K. M. Gierens (2009), Modelling of cirrus clouds – Part 1a: Model
978 description and validation, *Atmos. Chem. Phys.*, *9*, 685–706, doi:10.5194/acp-9-685-2009.

979 Stephens, G. L., D. O’Brien, P. J. Webster, P. Pilewski, S. Kato, and J.-I. Li (2015), The
980 albedo of Earth, *Rev. Geophys.*, *53*, 141–163, doi:10.1002/2014RG000449.

981 Stubenrauch, C. J., W. B. Rossow, S. Kinne, S. Ackerman, G. Cesana, H. Chepfer, L. D.
982 Girolamo, B. Getzewich, A. Guignard, A. Heidinger, B. C. Maddux, W. P. Menzel, P.
983 Minnis, C. Pearl, S. Platnick, C. Poulsen, J. Riedi, S. Sun-Mack, A. Walther, D. Winker, S.
984 Zeng, and G. Zhao (2013), Assessment of global cloud datasets from satellites. , *Bull.*
985 *Amer. Meteorol. Soc.*, *94*, 1031-1049, DOI:10.1175/BAMS-D-12-00117.1.

986 Unterstrasser, S., and K. Gierens (2010a), Numerical simulations of contrail-to-cirrus
987 transition - Part 2: Impact of initial ice crystal number, radiation, stratification, secondary
988 nucleation and layer depth, *Atmos. Chem. Phys.*, *10*, 2037-2051, doi:10.5194/acp-10-2037-
989 2010.

990 Unterstrasser, S., and K. Gierens (2010b), Numerical simulations of contrail-to-cirrus
991 transition - Part 1: An extensive parametric study, *Atmos. Chem. Phys.*, *10*, 2017-2036,
992 doi:10.5194/acp-10-2017-2010.

993 Unterstrasser, S., I. Sölch, and K. Gierens (2012), Cloud resolving modeling of contrail
994 evolution, in *Atmospheric Physics - Background - Methods - Trends*, edited by U.
995 Schumann, pp. 543-559, Springer, Heidelberg, doi: 10.11007/978-3-642-30183-4_33.

996 Unterstrasser, S. (2014), Large eddy simulation study of contrail microphysics and geometry
997 during the vortex phase and consequences on contrail-to-cirrus transition, *J. Geophys. Res.*
998 *Atmos.*, *119*, 7537-7555, doi:10.1002/2013JD021418.

999 Unterstrasser, S., and N. Görsch (2014), Aircraft-type dependency of contrail evolution, *J.*
1000 *Geophys. Res.*, *119*, 14015.

1001 Vay, S. A., B. E. Anderson, G. W. Sachse, J. E. Collins, J. R. Podolske, C. H. Twohy, B.
1002 Gandrud, K. R. Chan, S. L. Baughcum, and H. A. Wallio (1998), DC-8-based observations
1003 of aircraft CO, CH₄, N₂O, and H₂O(g) emission indices during SUCCESS, *Geophys. Res.*
1004 *Lett.*, *25*, 1717-1720, DOI: 10.1029/98GL00656.

1005 Vázquez-Navarro, M., B. Mayer, and H. Mannstein (2013), A fast method for the retrieval of
1006 integrated longwave and shortwave top-of-atmosphere upwelling irradiances from
1007 MSG/SEVIRI (RRUMS), *Atmos. Meas. Tech.*, *6*, 2627-2640, doi:10.5194/amt-6-2627-
1008 2013.

1009 Vázquez-Navarro, M., H. Mannstein, and S. Kox (2015), Contrail life cycle and properties
1010 from one year of MSG/SEVIRI rapid-scan images, *Atmos. Chem. Phys.*, [15](https://doi.org/10.5194/acp-15-8739-2015), 8739-8749,
1011 [doi:10.5194/acp-15-8739-2015](https://doi.org/10.5194/acp-15-8739-2015), ~~2015 *Disc.*, 15, 7019-7055, doi:10.5194/acpd-15-7019-~~
1012 ~~2015~~.

1013 Voigt, C., U. Schumann, P. Jessberger, T. Jurkat, A. Petzold, J.-F. Gayet, M. Krämer, T.
1014 Thornberry, and D. W. Fahey (2011), Extinction and optical depth of contrails, *Geophys.*
1015 *Res. Lett.*, *38*, L11806 doi:10.1029/2011GL047189.

1016 Voigt, C., A. Minikin, U. Schumann, and ML-CIRRUS_team (2015), ML-CIRRUS - the
1017 HALO mission on mid latitude cirrus clouds, *Geophysical Research Abstracts*, *17*,
1018 EGU2015-2758, <http://meetingorganizer.copernicus.org/EGU2015/EGU2015-2758.pdf>.

1019 Wang, M., and J. E. Penner (2010), Cirrus clouds in a global climate model with a statistical
1020 cirrus cloud scheme, *Atmos. Chem. Phys.*, *10*, 5449-5474, doi:10.5194/acp-10-5449-2010.

1021 Wilcox, L. J., K. P. Shine, and B. J. Hoskins (2012), Radiative forcing due to aviation water
1022 vapour emissions, *Atmos. Env.*, *63*, 1-13, doi: 10.1016/j.atmosenv.2012.08.072.

1023 Wilkerson, J. T., M. Z. Jacobson, A. Malwitz, S. Balasubramanian, R. Wayson, G. Fleming,
1024 A. D. Naiman, and S. K. Lele (2010), Analysis of emission data from global commercial
1025 aviation: 2004 and 2006, *Atmos. Chem. Phys.*, *10*, 6391-6408, doi:10.5194/acp-10-6391-
1026 2010.

1027 Yang, P., G. Hong, A. E. Dessler, S. S. C. Ou, K.-N. Liou, P. Minnis, and Harshvardhan
1028 (2010), Contrails and induced cirrus - optics and radiation, *Bull. Amer. Meteorol. Soc.*, *91*,
1029 473--478.

1030 Yi, B., P. Yang, K.-N. Liou, P. Minnis, and J. E. Penner (2012), Simulation of the global
1031 contrail radiative forcing: A sensitivity analysis, *Geophys. Res. Lett.*, *39*, DOI:
1032 10.1029/2012GL054042.

1033 Yun, Y., and J. E. Penner (2012), Global model comparison of heterogeneous ice nucleation
1034 parameterizations in mixed phase clouds, *J. Geophys. Res.*, *117*, 7203–7203,
1035 doi:10.1029/2011JD016506.

1036 Yun, Y., J. E. Penner, and O. Popovicheva (2013), The effects of hygroscopicity on ice
1037 nucleation of fossil fuel combustion aerosols in mixed-phase clouds, *Atmos. Chem. Phys.*,
1038 *13*, 4339–4348, doi:10.5194/acp-13-4339-2013.

1039 Zhang, Y., A. Macke, and F. Albers (1999), Effect of crystal size spectrum and crystal shape
1040 on stratiform cirrus radiative forcing, *Atmos. Res.*, *52*, 59-75, doi:10.1016/S0169-
1041 8095(99)00026-5.

Formatiert: Schriftart: (Standard)
Times New Roman

1042 Zhou, C., and J. E. Penner (2014), Aircraft soot indirect effect on large-scale cirrus clouds: Is
1043 the indirect forcing by aircraft soot positive or negative?, *J. Geophys. Res.*, DOI:
1044 10.1002/2014JD021914.

1045

1046 **Tables**

1047

1048 Table 1. Schematic run specification

Run	Coupling method	Emission amounts	Integration period
0	offline	nominal	30 years
1	online	nominal	30 years
2	online	100 × increased	1 year

1049

1050

1051

1052

1053

1054 Table 2. Annual and global mean contrail properties from run 0 and 1 with standard

1055 deviations σ of interannual fluctuations for run 1 and percentage difference relative to run 0.

Parameter	Run 0	Run 1	σ	Rel. diff/%
	Offline	Online		
Flight fraction with contrail formation	0.158	0.154	0.001	-3
Flight fraction in ice supersaturated air	0.074	0.068	0.001	-8
Number of contrails at a time	2926	2862	53	-2
Relative humidity over ice at contrail formation (%)	119	116	0.5	-4
Contrail optical depth tau in solar range	0.335	0.289	0.002	-14
Cover by contrails with tau>0.1 (%)	0.551	0.505	0.007	-8
Age of contrails (h)	1.9	2.0	0.01	5
Ice crystals in contrails (10^{12} m^{-1})	2.72	2.87	0.02	5
Ice particle number concentration (cm^{-3})	0.388	0.438	0.003	13
Ice water content (mg m^{-3})	10.6	7.5	0.05	-29
Effective radius (μm)	45.4	35.1	0.17	-23
Total H ₂ O mass inventory (Tg)	51.4	31.8	0.5	-38
Sedimentation distance in contrails (km)	0.713	0.734	0.008	3
Contrail RFLW in North Atlantic region (NAR) (W m^{-2})	1.05	0.88	0.06	-16
Contrail radiative forcing, longwave, RFLW (W m^{-2})	0.171	0.143	0.002	-16
Contrail radiative forcing, shortwave, RFSW (W m^{-2})	-0.096	-0.080	0.002	-17
Contrail radiative forcing, net, RFSW+RFLW (W m^{-2})	0.074	0.063	0.001	-14

1056

1057 Table 3. Contrail properties per length unit in run 1.

parameter	mean	median	mean for age < 0.5 h
H ₂ O mass emission (kg m ⁻¹)	6.56×10 ⁻³	4.80×10 ⁻³	6.34×10 ⁻³
volume (m ³ m ⁻¹)	6.62×10 ⁶	2.01×10 ⁶	1.15×10 ⁵
air mass (kg m ⁻¹)	2.54×10 ⁶	8.02×10 ⁵	4.23×10 ⁴
ice mass (kg m ⁻¹)	4.87×10 ¹	6.08×10 ⁰	1.13×10 ⁰
ice particles, N _{ice} (m ⁻¹)	2.89×10 ¹²	2.21×10 ¹²	3.99×10 ¹²
width (m)	8.14×10 ³	5.00×10 ³	7.92×10 ²
S=N _{ice} π r _{area} ² (m ² m ⁻¹)	1.11×10 ³	4.80×10 ²	1.39×10 ²
optical depth (τ) × width (m)	2.25×10 ³	1.06×10 ³	2.78×10 ²
ratio ice mass/H ₂ O mass emission	1.78×10 ⁶	1.78×10 ³	1.78×10 ²

1058

1059

1060 Table 4. Change in contrail properties for 100 times larger fuel consumption

1061

Parameter	Run 1 online	Run 2 100×fuel	Ratio runs 2/1
Fuel consumption in contrails (kg/km)	5.33	533	100
Ice crystals (10^{12} m^{-1})	2.87	272	94
Total ice mass inventory (Tg)	31.8	311	9.8
Sedimentation distance (m)	0.734	0.735	1.0
Age (h)	2.00	4.02	2.0
Width (km)	18.1	168	9.3
Effective depth (m)	829	2380	2.9
IWC (mg m^{-3})	7.5	3.1	0.42
Ice particle number concentration (cm^{-3})	0.438	2.70	6.2
Effective radius (μm)	35.1	13.0	0.37
Ice mass content (kg/m)	138	155	1.1
Ice mass content per H_2O emission (1)	21100	2350	0.11
Contrail net RF (W m^{-2})	0.063	0.87	13.81
Cover of contrails with $\tau > 0.1$ (%)	0.505	3.88	7.68
Optical depth of contrails with $\tau > 0.1$ (1)	0.367	1.375	3.75

1062

1063

1064

1065

1066

1067 Table 5. Annual and global mean CAM results for normal (run 1) and 100×fuel (run 2), with
 1068 standard deviations of interannual variability (σ).

1069

Abbreviation	Parameter	Run 1,		Run 2,		Unit
		mean	$\pm\sigma$	mean	$\pm\sigma$	
FSNT	SW net RF	0.077	0.301	0.272	0.190	W m ⁻²
FLNT	LW net RF	-0.007	0.181	-0.449	0.130	W m ⁻²
SWCF	SW cloud forcing	0.076	0.320	0.313	0.204	W m ⁻²
LWCF	LW cloud forcing	-0.017	0.132	-0.211	0.094	W m ⁻²
FSNTC	SW clear sky forcing	0.002	0.092	-0.042	0.062	W m ⁻²
FLNTC	LW clear sky forcing	0.010	0.112	-0.239	0.081	W m ⁻²
LWP	liquid water path	-0.201	0.778	-0.494	0.526	g m ⁻²
IWP	ice water path	-0.001	0.096	-0.186	0.071	g m ⁻²
WVM	water vapor path	0.011	0.086	-0.040	0.067	kg m ⁻²
CLDHGH	high-level cloud cover	-0.033	0.201	-0.642	0.103	%
CLDMED	mid-level cloud clover	-0.037	0.150	-0.241	0.123	%
CLDLOW	low-level cloud cover	-0.024	0.201	-0.365	0.131	%

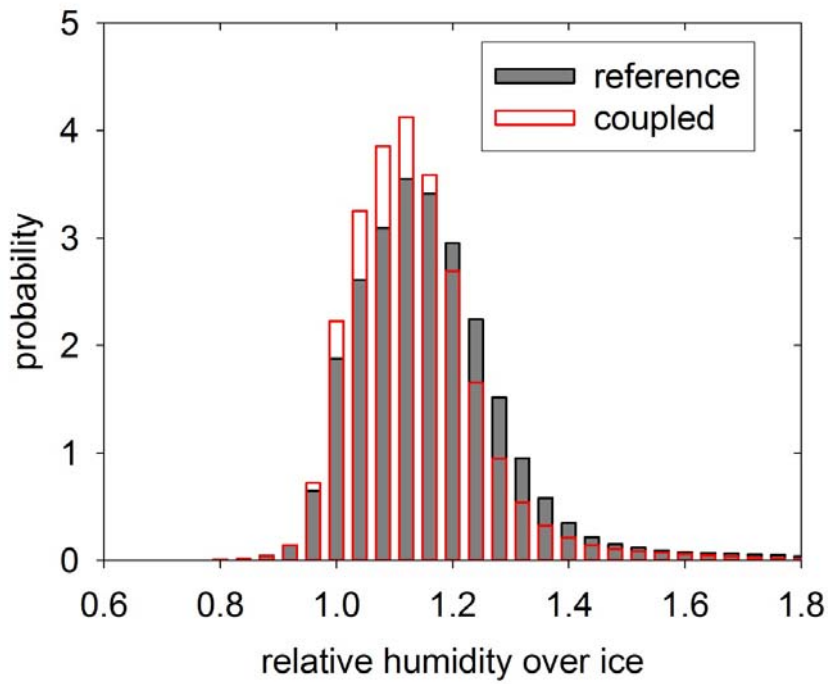
1070

1071

1072

1073 **Figures**

1074



1075

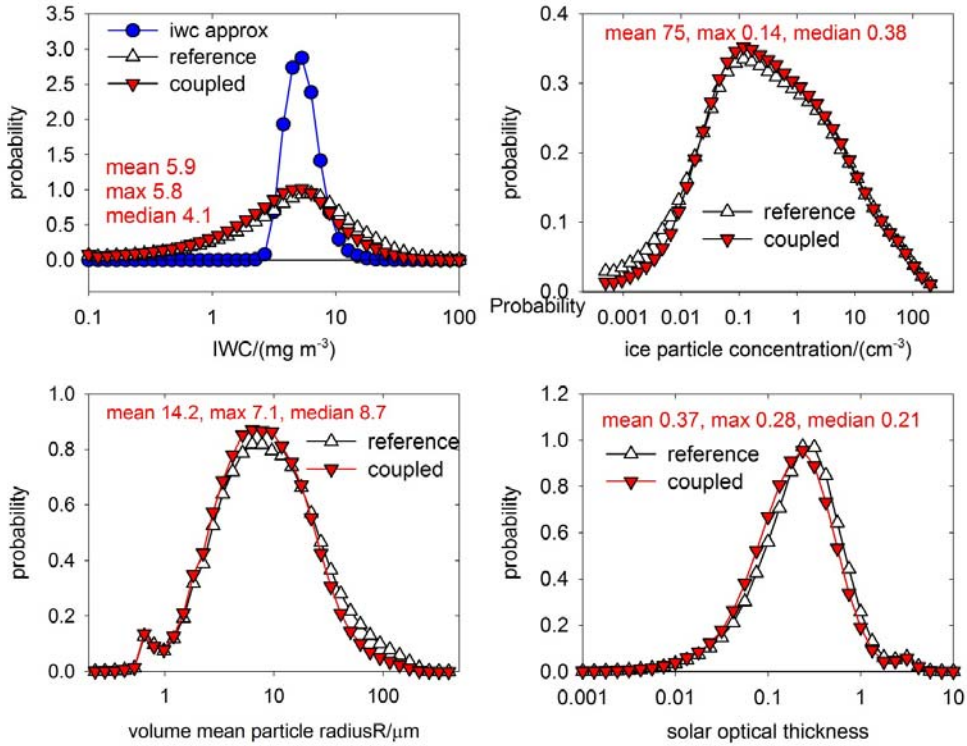
1076

1077 Figure 1. Probability density function (pdf) of relative humidity over ice in the freshly
1078 forming contrail segments without (black: reference case, run 0) and with (red: coupled, run
1079 1) humidity exchange.

1080

1081

1082

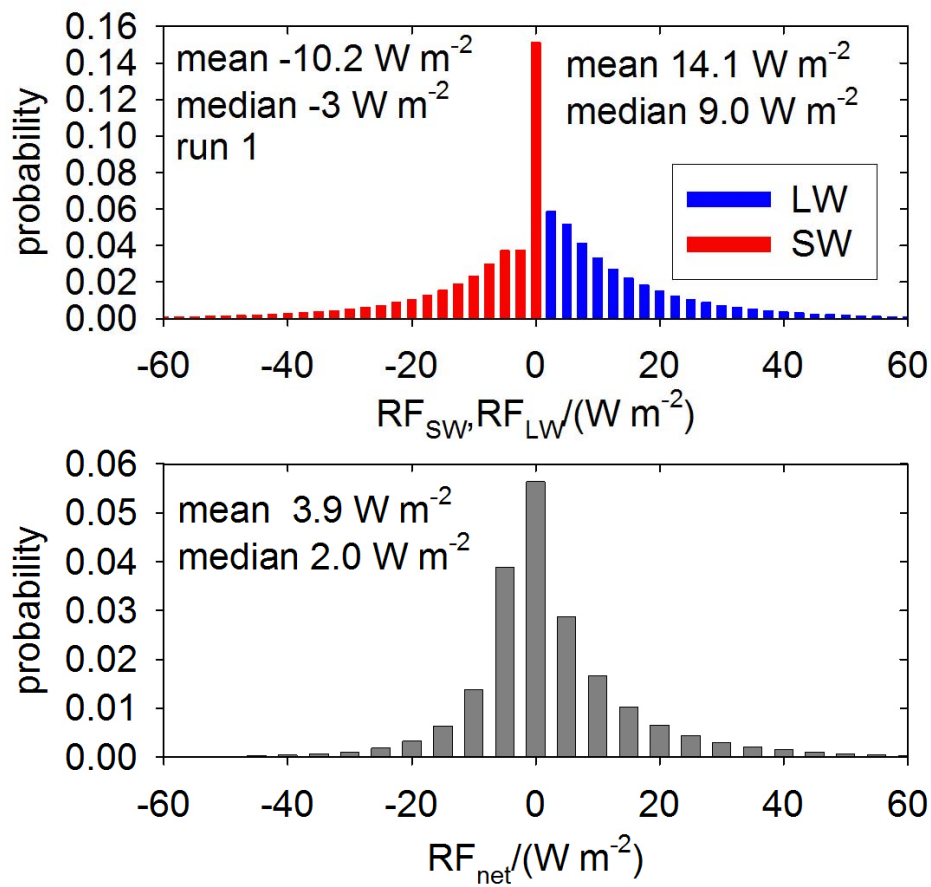


1083

1084

1085 Figure 2. Pdf of contrail properties from CoCiP-CAM for run 0 (white symbols: reference)
1086 and 1 (red symbols: coupled): ice water content IWC (blue: computed from temperature
1087 [Schumann, 2002]); ice particle concentration n_{ice} , volume mean particle radius r_{vol} , solar
1088 optical depth τ , all in logarithmic scales. Mean, median, and maximum-probability values are
1089 listed for run 1.

1090

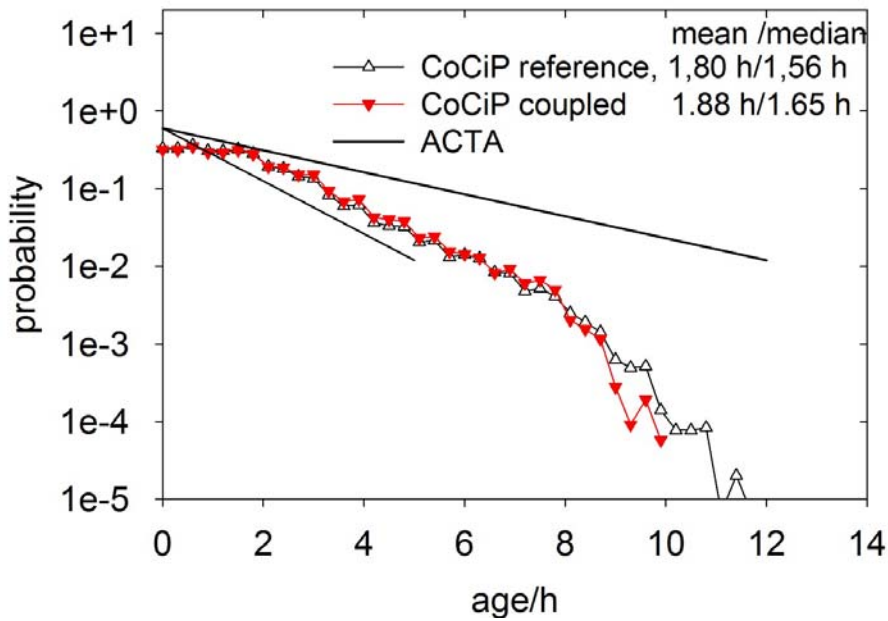


1091

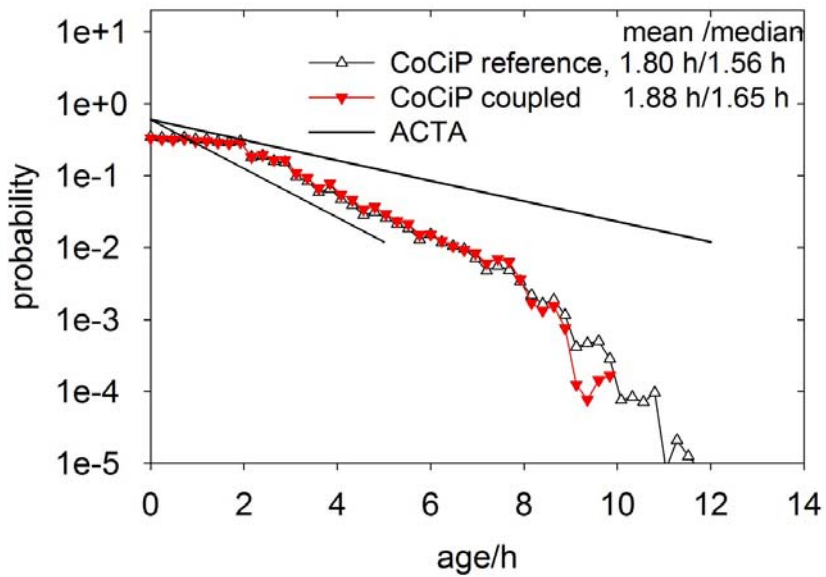
1092 | Figure 34. Pdf of local radiative forcing by contrails in the shortwave (red) and longwave
 1093 (blue) ranges (top), and net RF (bottom).

1094

1095



1096

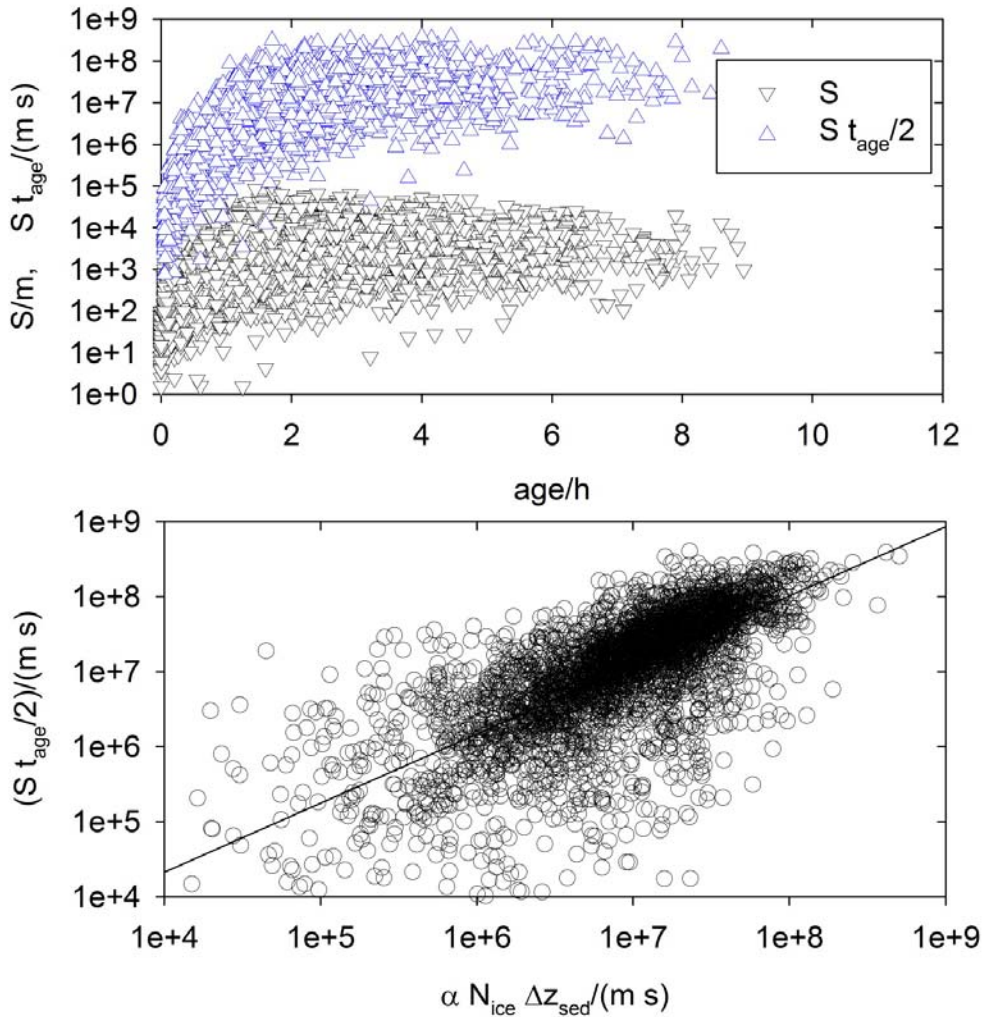


1097

1098 Figure 43. Pdf of contrail ages. Symbols for CoCiP runs 0 and 1 (significant below about 8 h
 1099 ages), with given mean/median values The straight lines enclose age results for contrails
 1100 tracked with the ACTA algorithm in infrared Meteosat data [Vázquez-Navarro *et al.*, 2015].

1101

1102

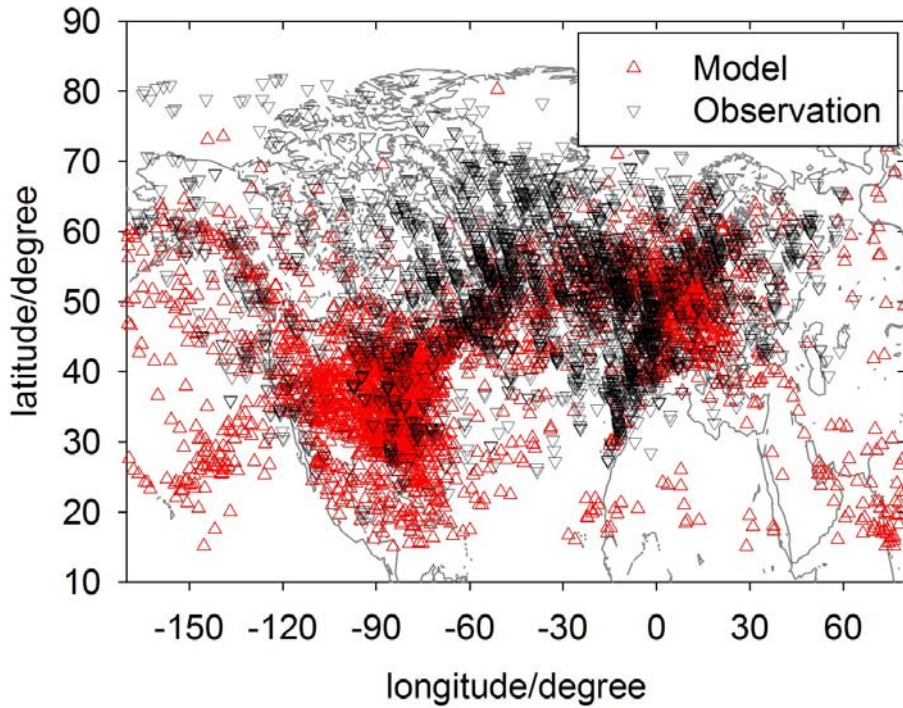


1103

1104 Figure 5. Ice particle cross section area S per contrail length (unit m^2/m) and its approximated
1105 time integral $\int S dt \cong S t_{\text{age}}/2$ (in m s) versus plume age t_{age} (top panel) and versus the
1106 approximating parameter suggested by Lewellen [2014] (see text). The line depicts a linear fit.

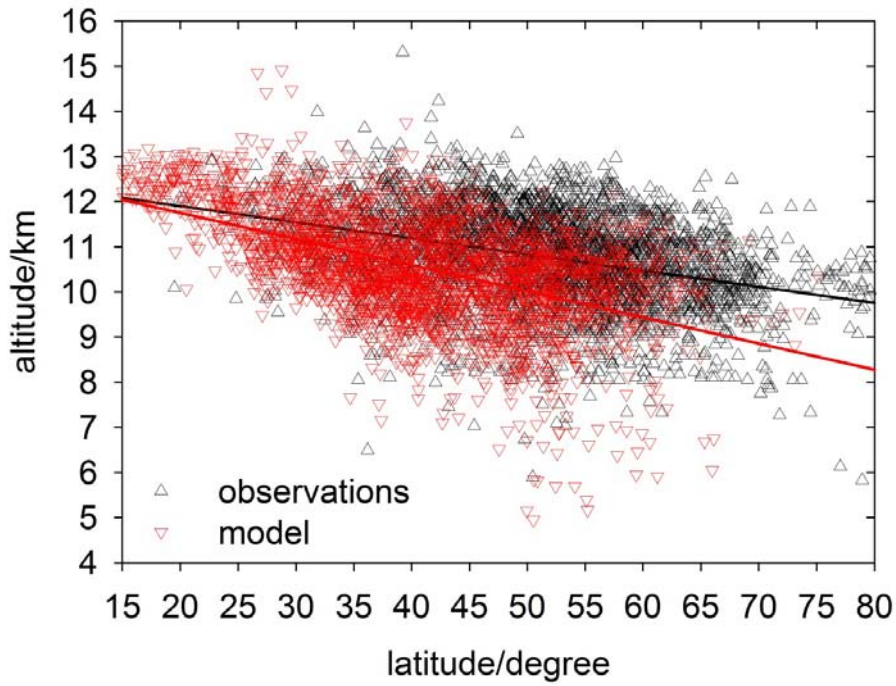
1107

1108



1109
 1110 Figure 6. Contrail occurrence computed with CoCiP-CAM (red upward triangles, run 1) and
 1111 analyzed from MODIS-CALIPSO observations (black downward triangles, data from
 1112 *Iwabuchi et al.* [2012]), for 180°W – 60°E, 15°N– 85°N. The triangles represent single
 1113 contrail events (a small random sub-set of computed contrails is plotted).
 1114

1115

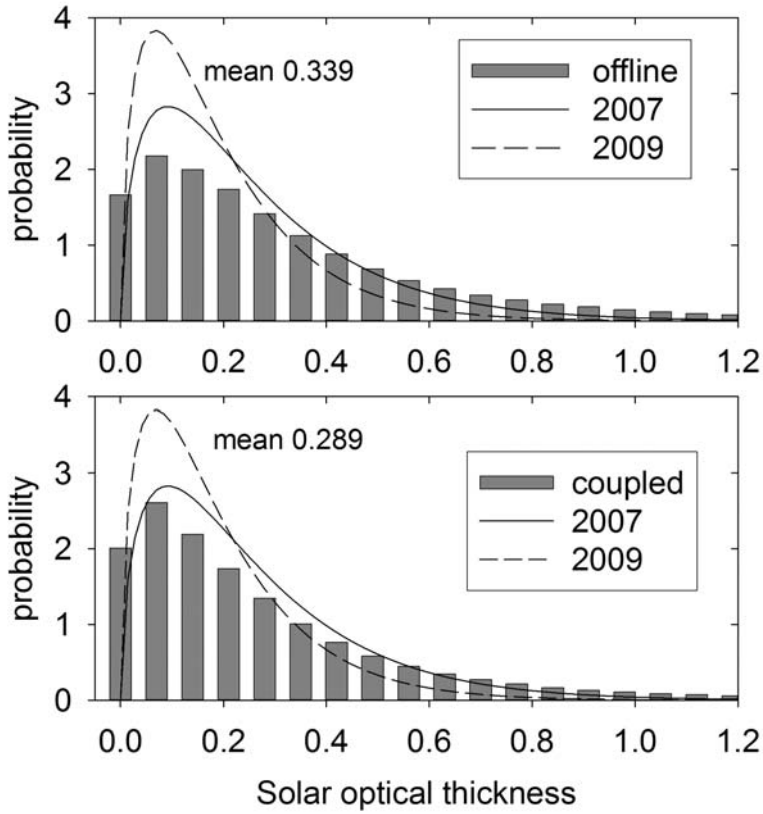


1116

1117 Figure 7. Contrail occurrence versus latitude as in Figure 6. Red symbols: CoCiP-CAM;
1118 black: MODIS-CALIPSO data from *Iwabuchi et al.* [2012]. The colored lines are linear fits to
1119 the respective data.

1120

1121

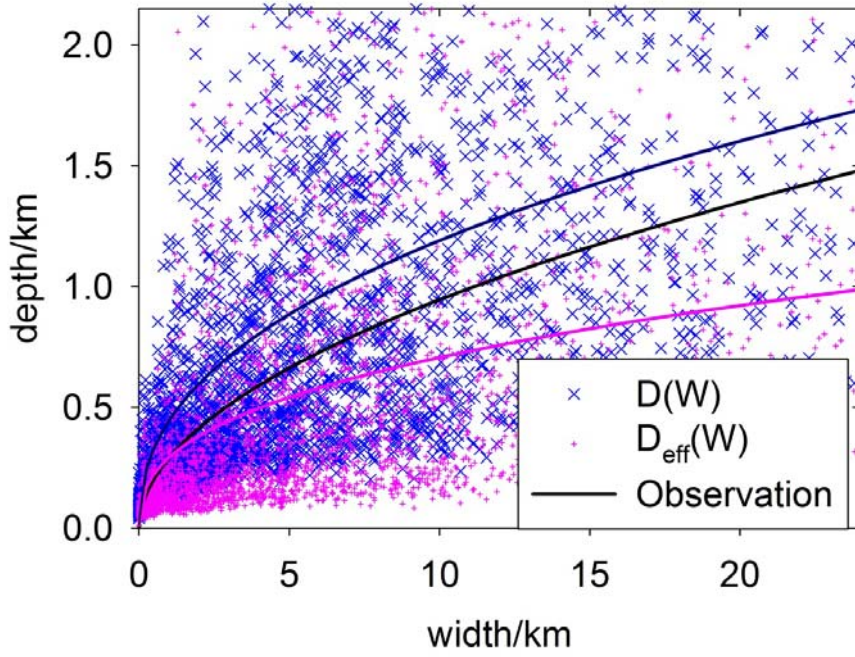


1122

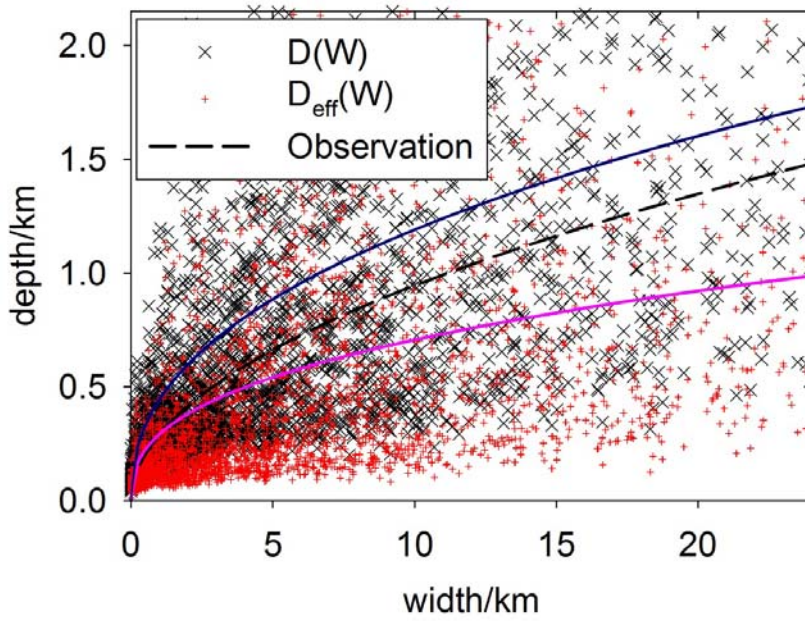
1123 Figure 8. Pdf of solar optical depth of contrails in CoCiP-CAM simulations. Top: run 0,
1124 bottom: run 1. The curves in both panels are the same and are Gamma functions
1125 approximating MODIS-CALIPSO observations in 2007 and 2009 (full and dashed), as
1126 reported by *Iwabuchi et al.* [2012].

1127

1128



1129

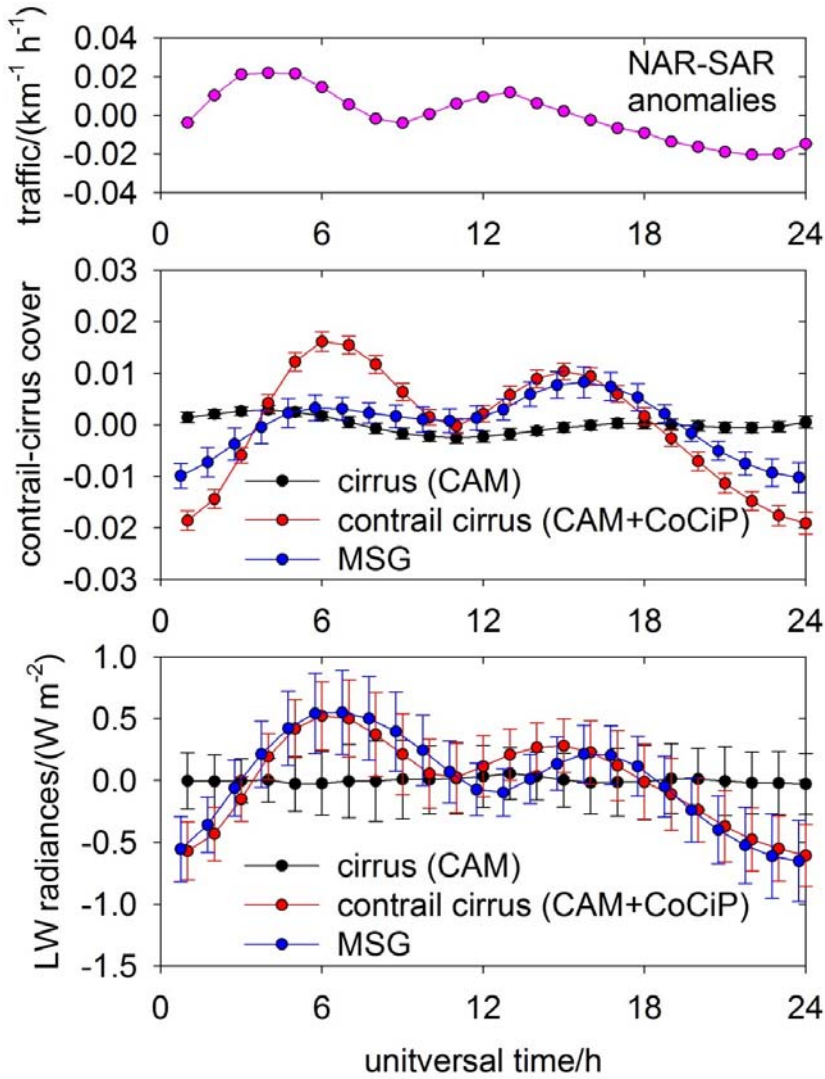


1130

1131 | Figure 9. Contrail Gaussian plume depth D (**blackue**), and effective depth D_{eff} (**redpurple**)
1132 | versus contrail width W from CoCiP/CAM. The crosses show individual contrail results in the
1133 | domain as in Figure 6. The blue/purple curves show power-law regression results, $D/\text{km}=0.68$
1134 | $(W/\text{km})^{0.373}$, and $D_{\text{eff}}/\text{km} = 0.454 (W/\text{km})^{0.420}$. The black **dashed** curve is the corresponding
1135 | regression $D/\text{km}= 0.29(W/\text{km})^{0.513}$ as given by *Iwabuchi et al.* [2012].

1136

1137



1138

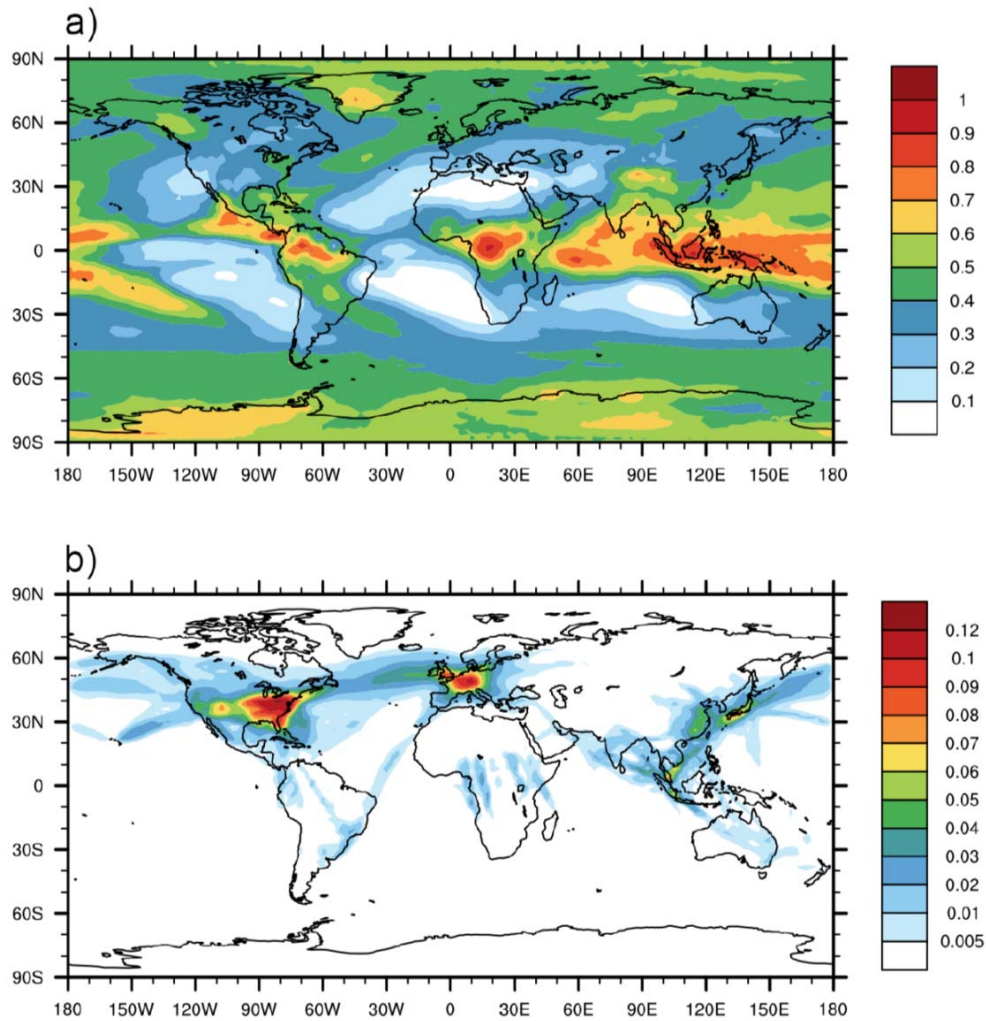
1139

1140 Figure 10. Diurnal cycle of anomalies of differences between a North Atlantic region and a
1141 South Atlantic region for air traffic density (top panel), cirrus cover (middle), and outgoing
1142 longwave radiation (bottom), versus universal time of day. The error bars denote the standard
1143 deviations of annual means. In the two lower panels, black symbols denote CAM results, red
1144 symbols the sum of CAM and CoCiP contributions, and blue symbols results derived from 8

1145 years of satellite (Meteosat second generation, MSG) infrared observations [*Graf et al.*, 2012;
1146 *Schumann and Graf*, 2013].

1147

1148

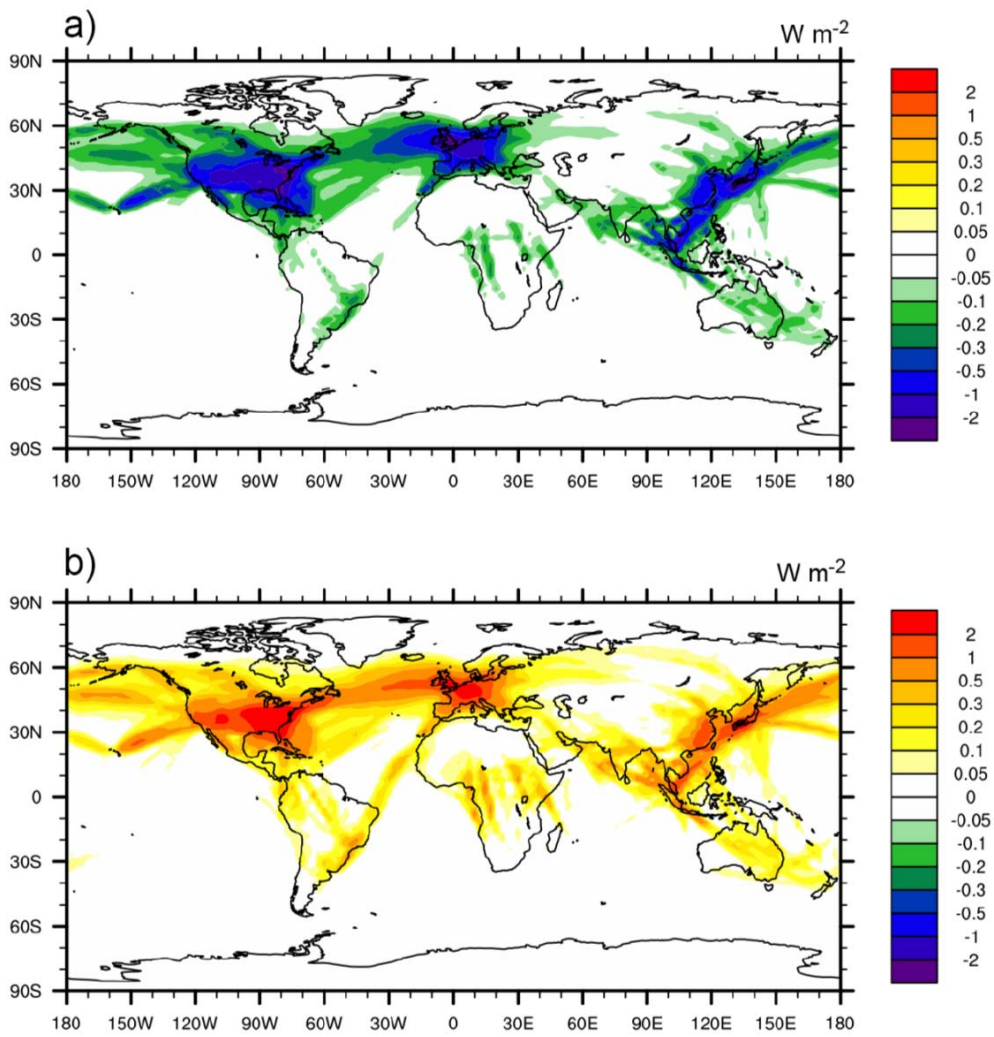


1149

1150

1151 Figure 11. a) Global map of annual mean cirrus cover (mean 0.40) and b) cover by contrails
1152 exceeding an optical depth (at 550 nm) of 0.1 (mean 0.0050).

1153



1154

1155

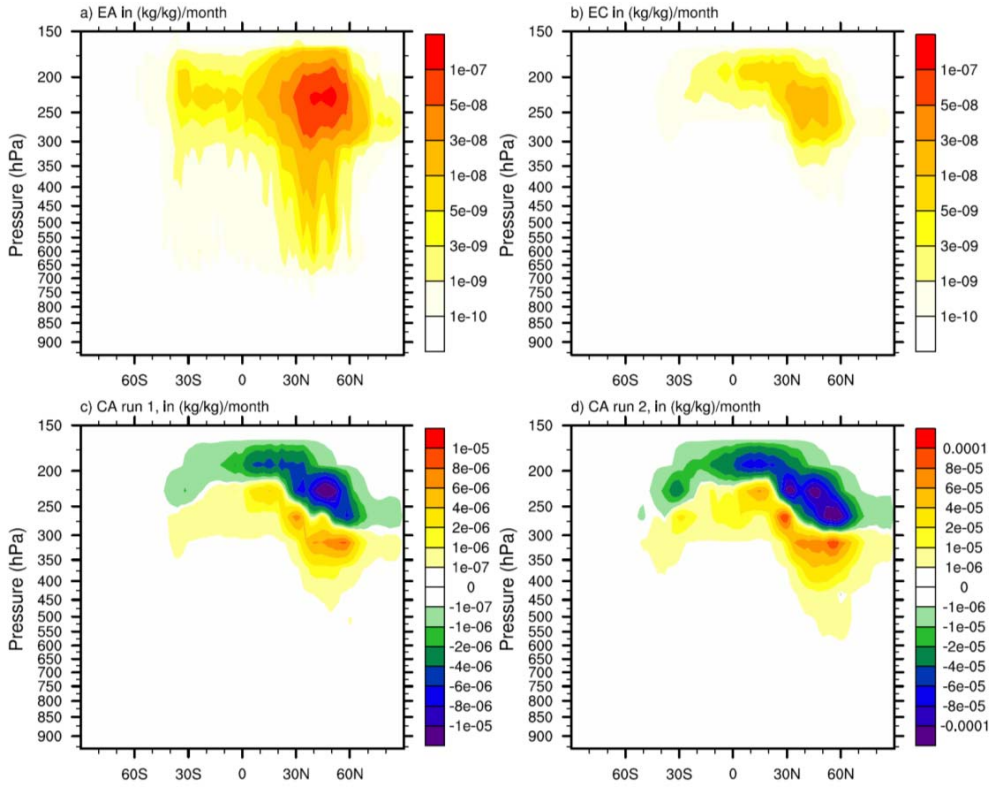
1156

1157 Figure 12. Global map of annual mean radiative forcing by contrails, a) SW (mean -0.080 W

1158 m^{-2}), b) LW (mean 0.143 W m^{-2}), in logarithmic color scales.

1159

1160



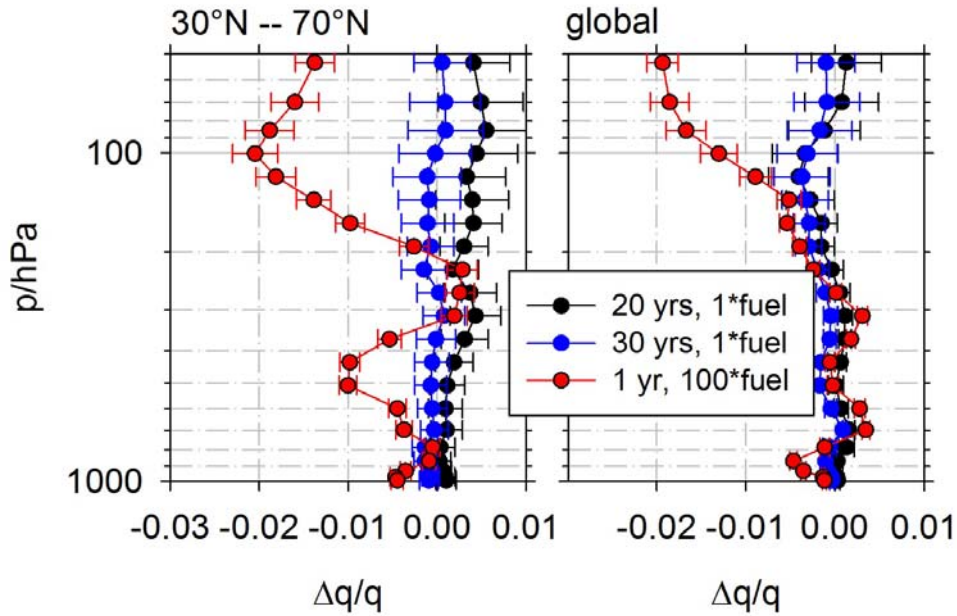
1161

1162 Figure 13. Zonal and annual mean water emission rates (in units of mass mixing ratio per
1163 time) versus latitude and pressure a) from aircraft engines directly into the free atmosphere
1164 (EA), b) from aircraft engines into contrails (EC), and c) from sublimating contrails into the
1165 atmosphere (CA, negative values mean water deposition on contrail ice), for run 1. Panel d)
1166 shows CA for run 2. Note different scales.

1167

1168

1169

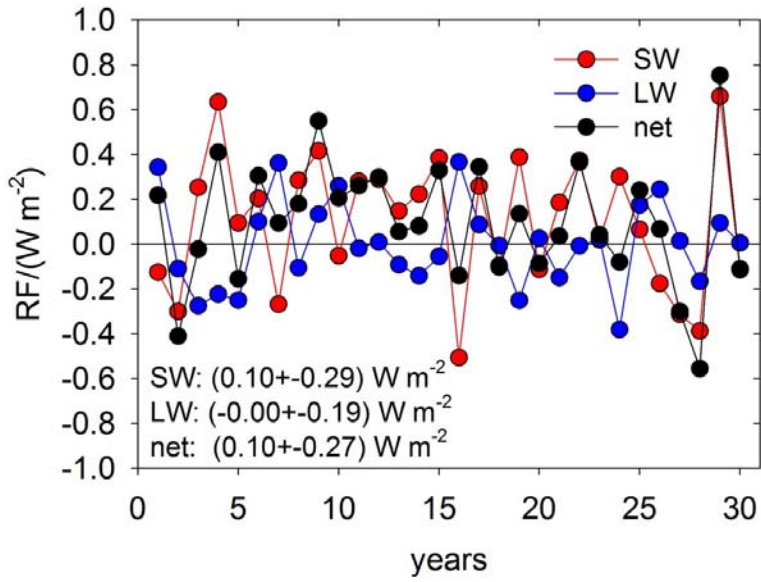


1170

1171 Figure 14. Vertical profiles of changes in normalized absolute humidity ($\Delta q/q$) from
1172 differences between run 1 or 2 and run 0 averaged over 20 (black), 30 (blue), 1 (red) years for
1173 the northern mid latitudes (left) and globally (right). Run 1 uses normal traffic, run 2 uses 100
1174 times increased fuel consumption. In this figure, error bars estimate significance limits from
1175 the root-mean-square variances divided by $\sqrt{(N-2)}$, where N is the number of years available
1176 for averaging.

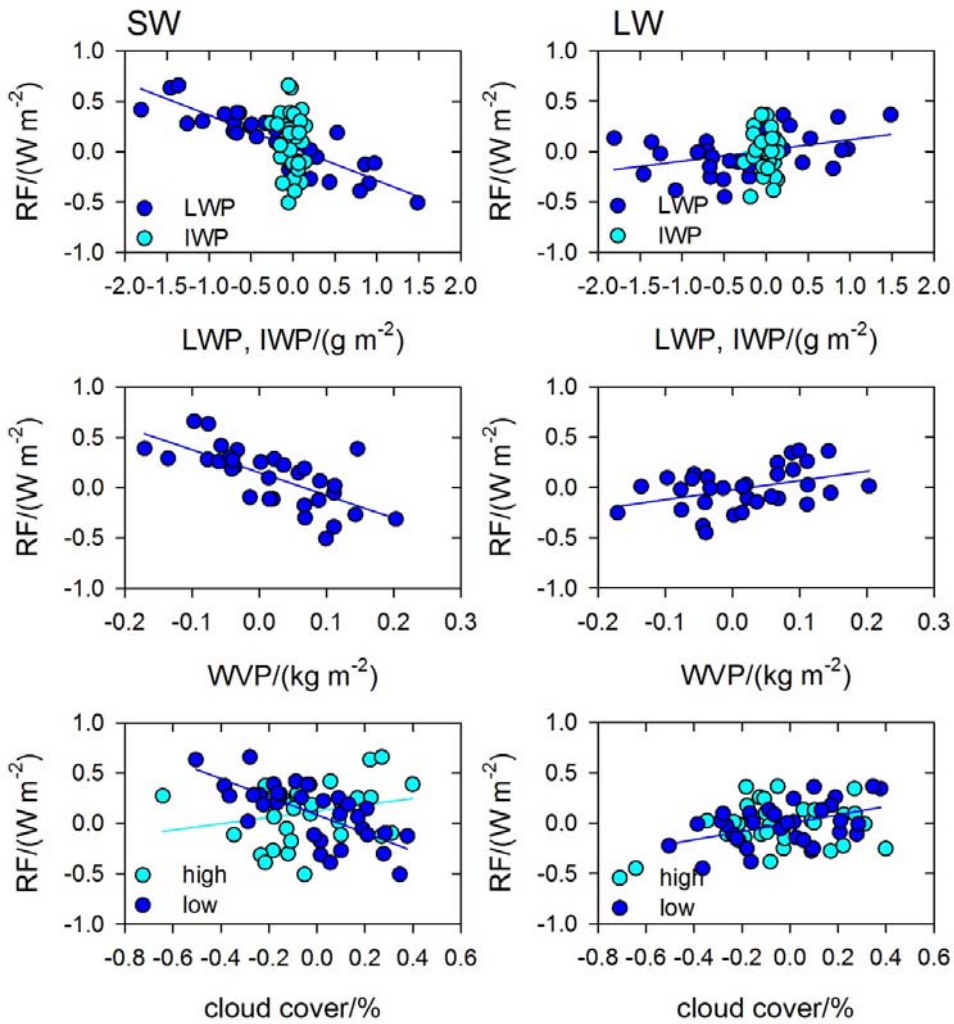
1177

1178



1179

1180 Figure 15. Annual and global mean shortwave (SW), longwave (LW) and net (SW+LW)
1181 radiative forcing (RF) from dehydration by contrails, as reflected in CAM by the net top of
1182 the atmosphere radiance difference run 1-run 0, versus years.



1184

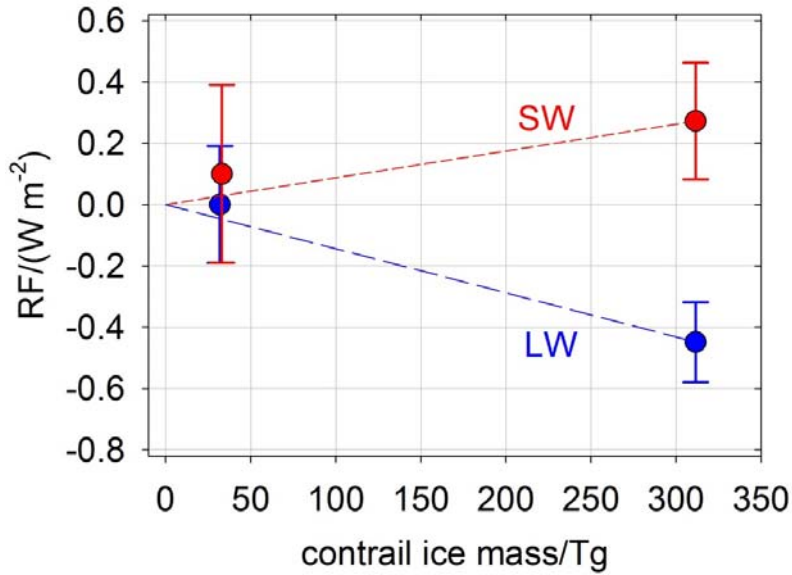
1185

1186 Figure 16. SW (left panels) and LW (right) RF correlations with liquid and ice water path
 1187 (LWP, IWP), water vapor path (WVP), and high and low-level cloud cover in annual mean
 1188 values of the differences of CAM results in run 1 and run 0.

1189

1190

1191



1192

1193 Figure 17. SW and LW RF from humidity redistribution by contrails in CAM for nominal
1194 (run 1 - run 0) or 100 times increased air traffic emissions (run 2 - run 0) as a function of
1195 global ice mass in contrails. The error bars denote the standard deviations of interannual
1196 fluctuations; for run 2 these are computed from 30 years of run 0 and one year of run 2
1197 results. The red/blue lines indicate linear interpolations between zero and SW/LW RF results
1198 from run 2.